J. Fluid Mech. (2011), *vol.* 688, *pp.* 120–168.
doi:10.1017/jfm.2011.368

Turbulence in supersonic boundary layers at moderate Reynolds number

Sergio Pirozzoli† and Matteo Bernardini

Dipartimento di Ingegneria Meccanica e Aerospaziale, Università di Roma 'La Sapienza', via Eudossiana 18, 00184 Roma, Italy

(Received 24 March 2011; revised 6 July 2011; accepted 1 September 2011; first published online 21 October 2011)

We study the organization of turbulence in supersonic boundary layers through large-scale direct numerical simulations (DNS) at $M_\infty = 2$, and momentum-thickness Reynolds number up to $Re_{\delta_2} \approx 3900$ (corresponding to $Re_\tau \approx 1120$) which significantly extend the current envelope of DNS in the supersonic regime. The numerical strategy relies on high-order, non-dissipative discretization of the convective terms in the Navier–Stokes equations, and it implements a recycling/rescaling strategy to stimulate the inflow turbulence. Comparison of the velocity statistics up to fourth order shows nearly exact agreement with reference incompressible data, provided the momentum-thickness Reynolds number is matched, and provided the mean velocity and the velocity fluctuations are scaled to incorporate the effects of mean density variation, as postulated by Morkovin's hypothesis. As also found in the incompressible regime, we observe quite a different behaviour of the second-order flow statistics at sufficiently large Reynolds number, most of which show the onset of a range with logarithmic variation, typical of 'attached' variables, whereas the wall-normal velocity exhibits a plateau away from the wall, which is typical of 'detached' variables. The modifications of the structure of the flow field that underlie this change of behaviour are highlighted through visualizations of the velocity and temperature fields, which substantiate the formation of large jet-like and wake-like motions in the outer part of the boundary layer. It is found that the typical size of the attached eddies roughly scales with the local mean velocity gradient, rather than being proportional to the wall distance, as happens for the wall-detached variables. The interactions of the large eddies in the outer layer with the near-wall region are quantified through a two-point amplitude modulation covariance, which characterizes the modulating action of energetic outer-layer eddies.

Key words: boundary layer structure, compressible boundary layers, turbulent boundary layers

1. Introduction

The prediction of turbulent high-speed wall-bounded flows remains an active field of study for its technological importance in the aerospace industry. In this respect, a major role has been historically played by experiments, whereas direct numerical simulations (DNS) and large-eddy simulations (LES) have only become common

† Email address for correspondence: sergio.pirozzoli@uniroma1.it

in the last decade or so. A considerable amount of work has been devoted to the understanding of the canonical zero-pressure-gradient boundary layer flow, which is itself a challenging task. Indeed, boundary layers by their nature are spatially developing flows, and their structure is strongly sensitive to the particular strategy used to enforce the boundary conditions at the computational inflow. As recently shown through DNS in the incompressible regime (Simens *et al.* 2009), and previously observed in experiments (Erm & Joubert 1991), the achievement of a fully developed state of the boundary layer (and thus the correct prediction of the turbulent boundary layer statistics) requires the use of extremely long computational domains (in excess of fifty boundary layer thicknesses), which makes accurate numerical simulations extremely computationally demanding.

Numerical simulations of wall-bounded turbulent flows in the supersonic regime are further slowed down by the inherently larger computational effort, and by the possible occurrence of shock waves, either in the form of external disturbing elements (such as in shock wave/boundary layer interactions), or embedded in turbulence ('eddy shocklets'). Therefore, the overwhelming majority of the computational algorithms designed for LES and DNS of compressible flows rely on some form of upwinding or explicit filtering (and dealiasing in spectral simulations) for numerical stabilization, and most often incorporate some form of shock-capturing, which implies the introduction of additional numerical dissipation. As a consequence, although the fine grid spacings used in DNS generally guarantee adequate representation of the gross flow features, the small-scale structures may be poorly resolved. Also, most previous numerical studies performed in the supersonic regime are based on simplifying assumptions to relate the spatial growth of the boundary layer with its temporal growth in the presence of streamwise periodic boundary conditions (Guarini *et al.* 2000; Maeder, Adams & Kleiser 2001; Martín 2007). Other studies rely on the idea of following the entire process of boundary layer transition starting from laminar inflow conditions into the fully developed region (Pirozzoli, Grasso & Gatski 2004), or on the extension of Lund's recycling–rescaling technique (Stolz & Adams 2003; Xu & Martin 2004; Lagha *et al.* 2011).

While the dynamics of the near-wall layer are sufficiently well understood (Jiménez & Pinelli 1999), recent studies (Hutchins & Marusic 2007) have highlighted the occurrence of new physical mechanisms when the Reynolds number becomes sufficiently high, which involve the interaction of energetically significant outer-layer structures with the inner part of the boundary layer. Under such conditions an energy peak emerges in the logarithmic part of the boundary layer, associated with the appearance of large, streaky structures, that may be extremely long, and that are currently referred to as 'superstructures'. The presence of superstructures in supersonic high-Reynolds-number boundary layers was documented in the experiments of Ganapathisubramani, Clemens & Dolling (2006), and confirmed in the numerical study of Ringuette, Wu & Martín (2008). The large-scale motions in the outer layer are regarded to be responsible for the increase of the turbulence intensities (when reported in inner scaling) with the Reynolds number (Hoyas & Jiménez 2006), and for the modulation of the fine-scale near-wall turbulence (Mathis, Hutchins & Marusic 2009*a*). We note that, owing to difficulties in obtaining the full spatial information in experiments, the detection of superstructures mostly relies on the analysis of time signals at a given position, exploiting Taylor's hypothesis, whose validity may be questionable when applied to large-scale structures (Jiménez *et al.* 2010). Notable exceptions to this statement include the tomographic particle image velocimetry experimental data by Humble *et al.* (2009) and Elsinga *et al.* (2010), which provide insight into the full instantaneous three-dimensional structure of the flow field.

The discovery of the superstructures has stimulated a series of large-scale direct numerical simulations of low-speed boundary layers (Wu & Moin 2009; Jiménez *et al.* 2010; Schlatter & Örlü 2010*a*), aiming to probe the behaviour of wall turbulence at high Reynolds numbers. No such attempt has been made in this direction for supersonic wall-bounded flows. The main purpose of the present paper is to fill this gap, and provide accurate information on the behaviour of supersonic turbulent boundary layers at (computationally) high Reynolds number. In order to achieve this goal we have tried to minimize any source of numerical uncertainty, and developed a numerical algorithm that with good approximation is free from spurious dissipation errors and imprint from the numerical upstream conditions. The flow conditions considered in this study correspond to free-stream Mach number $M_\infty = 2$, and Reynolds number based on the local momentum thickness and wall viscosity (Fernholz & Finley 1976) $Re_{\delta_2} = \rho_\infty u_\infty \theta / \overline{\mu}_w$ from 560 to 3900, corresponding to friction Reynolds numbers $Re_\tau = \overline{\rho}_w u_\tau \delta / \overline{\mu}_w$ from 200 to 1120. The relatively low Mach numbers under consideration prevent the emergence of strong compressibility effects with subsequent formation of turbulent shocklets, which would require the use of some artificial dissipation to be captured. The range of Reynolds numbers considered extends from conditions typical of previous studies, into the range accessible from experiments, with which this work is intended to provide a bridge.

The paper is organized as follows. In § 2 the numerical strategy and the DNS database are described; the primary turbulence statistics are presented and compared with a wide body of available experimental data in § 3; the large-scale organization of the flow is illustrated in § 4; the statistical organization of the turbulent eddies (in terms of size and orientation) is addressed in § 5; the inner/outer layer interactions are quantified in terms of amplitude modulation in § 6; the relationships between the velocity and temperature fluctuating fields (strong Reynolds analogies) are investigated in § 7; concluding remarks are given in § 8.

2. Numerical methodology

We solve the three-dimensional Navier–Stokes equations for a perfect compressible gas

$$\frac{\partial \rho}{\partial t} + \frac{\partial (\rho\, u_j)}{\partial x_j} = 0, \tag{2.1a}$$

$$\frac{\partial (\rho u_i)}{\partial t} + \frac{\partial (\rho\, u_i u_j)}{\partial x_j} + \frac{\partial p}{\partial x_i} - \frac{\partial \sigma_{ij}}{\partial x_j} = 0, \tag{2.1b}$$

$$\frac{\partial (\rho E)}{\partial t} + \frac{\partial (\rho u_j E + p u_j)}{\partial x_j} - \frac{\partial (\sigma_{ij} u_i - q_j)}{\partial x_j} = 0, \tag{2.1c}$$

where ρ is the density, u_i $(i = 1, 2, 3)$ is the velocity component in the ith coordinate direction, E is the total energy, p and T the thermodynamic pressure and temperature, respectively. The set of the conservation equations is closed with the constitutive relations for a Newtonian fluid, whereby the heat flux vector q_j and the viscous stress tensor σ_{ij} are prescribed as

$$q_j = -k \frac{\partial T}{\partial x_j}, \tag{2.2a}$$

$$\sigma_{ij} = 2\,\mu S_{ij} - \tfrac{2}{3}\,\mu\, S_{kk}\, \delta_{ij}, \tag{2.2b}$$

where $S_{ij} = (u_{i,j} + u_{j,i})/2$ is the strain-rate tensor, μ is the molecular viscosity (assumed to depend on temperature through Sutherland's law) and $k = c_p \mu / Pr$ is the thermal conductivity (the molecular Prandtl number is set to $Pr = 0.72$).

The Navier–Stokes equations are discretized on a Cartesian mesh and solved by means of a conservative finite-difference approach. The flow solver relies on central sixth-order discretization of the convective terms of the Navier–Stokes equations cast in fully split form (Kennedy & Gruber 2008)

$$\frac{\partial \rho u_j \varphi}{\partial x_j} = \frac{1}{4}\frac{\partial \rho u_j \varphi}{\partial x_j} + \frac{1}{4}\left(u_j \frac{\partial \rho \varphi}{\partial x_j} + \rho \frac{\partial u_j \varphi}{\partial x_j} + \varphi \frac{\partial \rho u_j}{\partial x_j}\right) + \frac{1}{4}\left(\rho u_j \frac{\partial \varphi}{\partial x_j} + \rho \varphi \frac{\partial u_j}{\partial x_j} + u_j \varphi \frac{\partial \rho}{\partial x_j}\right), \tag{2.3}$$

where φ stands for any transported quantity in (2.1), being unity for the continuity equation, u_i $(i = 1, 2, 3)$ for the momentum equation, $h_0 = \gamma/(\gamma - 1)\, p/\rho + u^2/2$ (where γ is the specific heat ratio) for the total energy equation. As shown by Pirozzoli (2010), this arrangement leads to a locally conservative formulation, and guarantees discrete conservation of the total kinetic energy in the limit case of inviscid, incompressible flow, and also in the presence of grid stretching in the coordinate directions. The approach allows robust spatial discretization of the convective terms without the addition of spurious numerical dissipation in the form of upwinding or filtering, as customary in numerical simulations of compressible flows. When cast in locally conservative form, the method guarantees excellent computational efficiency, and it makes hybridization with shock-capturing methods straightforward (Bernardini, Pirozzoli & Grasso 2011). The diffusive terms in the Navier–Stokes equations are expanded to Laplacian form for improved numerical stability, and approximated with sixth-order central difference formulas, to guarantee proper action of molecular viscosity at the smallest scales resolved on the computational mesh. The resulting semi-discrete system of equations is advanced in time by means of a standard, fully explicit fourth-order Runge–Kutta algorithm.

The database analysed in the present paper is obtained from three distinct direct numerical simulations (hereafter referred to as TBL1, TBL2 and TBL3) of a spatially developing zero-pressure-gradient supersonic turbulent boundary layer with free-stream Mach number $M_\infty = 2$, at Reynolds number from low to moderate. Several relevant Reynolds numbers can be defined in compressible boundary layers, owing to the strong variation of the thermodynamic properties (Smits & Dussauge 2006). The best candidate to scale out the effects of compressibility is the Reynolds number based on the momentum thickness and the wall viscosity (Fernholz & Finley 1976), Re_{δ_2}, which reduces to the conventional momentum thickness in the incompressible limit, and which here covers the range 560–3900 (see table 2). Another relevant Reynolds number, which is often quoted in studies of low-speed boundary layers is the friction Reynolds number, Re_τ, giving the ratio between outer and inner length scales, and which here covers the range 200–1120. All computations have been performed in a long domain, which extends for $L_x = 106\,\delta_{in}$, $L_y = 8.3\,\delta_{in}$, $L_z = 9.6\,\delta_{in}$ in the streamwise (x), wall-normal (y) and spanwise (z) directions, δ_{in} being the boundary layer thickness at the inflow station. Additional details on the properties of the computational mesh are given in table 1, showing that the spacing in terms of wall units is sufficiently small to virtually resolve all the energetically relevant flow scales throughout the wall layer. Further confirmation of the adequacy of the mesh used for the DNS stems from inspection of the spectral densities of the streamwise velocity field (E_{uu}), reported in

https://doi.org/10.1017/jfm.2011.368 Published online by Cambridge University Press

	$Re_{\delta_{in}}$	N_x	N_y	N_z	Δx^+	Δy^+_δ	Δz^+	$T_0 u_\infty/\delta_{in}$	$T_f u_\infty/\delta_{in}$	L_{av}/δ
TBL1	4 736	1920	171	200	5.22–4.95	4.72–6.51	4.51–4.27	149.9	2258.5	0.60
TBL2	12 662	4160	221	440	5.86–5.58	9.42–12.35	4.99–4.75	90.8	423.9	0.75
TBL3	29 597	7680	331	800	6.84–6.57	11.72–15.50	5.91–5.67	128.1	370.9	0.35

TABLE 1. Summary of computational parameters for the DNS study. $Re_{\delta_{in}}$ is the Reynolds number based on the inflow boundary layer thickness. Δy^+_δ is the spacing in the wall-normal direction at the edge of the boundary layer. For all simulations the first point off the wall is located at a distance $\Delta y^+_w \approx 0.7$. T_0 and T_f are the initial and final time considered for collecting flow samples. L_{av} is the half-width of the interval used for statistical averaging in the streamwise direction. Wall units and local boundary layer thickness are taken at the reference stations listed in table 3.

Dataset	Re_τ	Re_θ	Re_{δ_2}	H	$C_f(\times 10^3)$
TBL1	205–273	872–1242	557–793	3.13–3.07	3.42–3.07
TBL2	448–591	2082–2921	1327–1863	2.99–2.97	2.76–2.50
TBL3	843–1123	4430–6071	2827–3878	2.93–2.90	2.28–2.10

TABLE 2. Global flow properties determined from the DNS study. The range of values refers to the second half of the computational domain, past the recycling station. $Re_\theta = \rho_\infty u_\infty \theta/\mu_\infty$; $Re_{\delta_2} = \rho_\infty u_\infty \theta/\overline{\mu}_w$; $Re_\tau = \overline{\rho}_w u_\tau \delta/\overline{\mu}_w$; $H = \delta^*/\theta$.

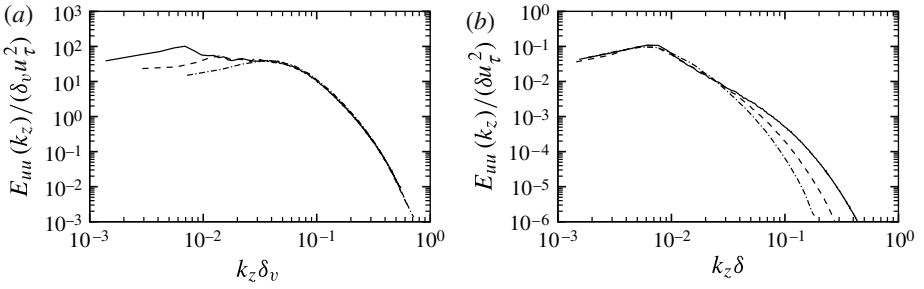

FIGURE 1. Spectral densities of streamwise velocity fluctuations in the spanwise direction at $y^+ = 15$ in inner scaling (a), and at $y/\delta = 0.2$ in outer scaling (b). See table 3 for line legend.

figure 1 as a function of the spanwise wavenumber (k_z). The spectra do not exhibit any energy pile-up at the high-wavenumber end which, given the absence of any numerical energy drain in the solver, indicates that all the flow scales are properly resolved. The figure further shows excellent collapse of the spectra at high wavenumbers when inner scaling is used, and at low wavenumbers when the outer scaling is used. The spectral peak observed in figure 1(a) at low wavenumbers for the high-Re simulations is the signature of an imprint of the outer-layer eddies on the near-wall region, which will be elaborated further on.

The boundary conditions at the upper and outflow boundaries are specified by unsteady characteristic decomposition in the direction normal to the boundary (Poinsot & Lele 1992), and setting to zero the time variation of the incoming waves to minimize reflection of spurious disturbances back into the computational domain. A characteristic wave decomposition is also used at the no-slip wall, where perfect reflection of acoustic waves is enforced, and the wall temperature is held fixed to its nominal adiabatic value ($T_{aw}/T_\infty = 1 + r(\gamma - 1)/2\,M_\infty^2$, the recovery factor being set to $r = Pr^{1/3}$). The flow is assumed to be statistically homogeneous in the spanwise direction, along which numerical periodicity is enforced. The two-point correlations in the spanwise direction (also see § 5) do not highlight any obvious coherent dynamics associated with finite computational span, supporting the adequacy of the size of the computational domain.

Particular attention has been devoted to the correct prescription of the inflow boundary conditions, which is a key ingredient in the simulation of spatially developing turbulent flows. As shown by Simens *et al.* (2009), the characteristic spatial scale for complete boundary layer decorrelation is approximately 30–50 boundary layer thicknesses, which mandates the use of extremely long computational domains. In the present study the inflow conditions are prescribed through a recycling–rescaling

procedure, suitably adapted to the compressible case (Pirozzoli, Bernardini & Grasso 2010*a*), and the recycling station is placed at $x_{rec} = 53\,\delta_{in}$ downstream of the inflow station, which is sufficient to achieve full decorrelation from the inflow, as testified from inspection of the streamwise two-point correlations, as was also done by Simens *et al.* (2009). The analysis (not reported) shows that the first half of the domain is contaminated by (although minimal) spurious numerical correlation. Consequently, the flow statistics are only collected in the second half of the domain ($x > x_{rec}$), where they are believed to be free from numerical artifacts.

A note of caution must also be issued regarding the sample used for the collection of the flow statistical properties. First, we must point out that a long initial transient of the simulations must be discarded for statistical purposes, during which turbulence spontaneously rearranges to an equilibrium state. In our experience a good indicator to check the establishment of equilibrium is the boundary layer shape factor ($H = \delta^*/\theta$, where δ^* is the displacement thickness, and θ is the momentum thickness). In the supersonic case the initial transient is relatively short compared to subsonic boundary layer simulations, given the virtual absence of feedback waves from the computational outlet, and we have found that, with proper specification of the recycling procedure, a period $T_0 \approx 100\delta_{in}/u_\infty$ is sufficient. After the end of the initial transient, equally spaced time samples of the full flow field have been collected at time intervals $\Delta t \approx 1.5\delta_{in}/u_\infty$, to guarantee a satisfactory degree of decorrelation between consecutive samples. Since the boundary layer is spatially developing, homogeneity in the streamwise direction in principle cannot be exploited, unlike for channel flows. This implies the need to collect many more time samples of the flow. However, to keep the computational effort within reasonable bounds, we decided to perform averaging of the flow statistics at a given station (say x_0) over a small surrounding streamwise interval ($-L_{av} \lesssim (x - x_0) \lesssim L_{av}$, where $L_{av} \approx \delta$). As shown by Jiménez *et al.* (2010), streamwise averaging alleviates the effect of numerical noise while not introducing significant statistical errors, given the slow streamwise growth of the boundary layer. Further details on the properties of the statistical ensemble are given in table 1.

We note that the TBL3 dataset (which includes a total of over two billion points) significantly extends the *Re* envelope of compressible boundary layer DNS, coming very close in terms of momentum thickness and friction Reynolds number to the landmark incompressible boundary layer simulation of Schlatter & Örlü (2010*a*), which is hereafter used as a primary low-speed reference for comparison. To our knowledge, previous compressible DNS studies were limited to $Re_{\delta_2} \lesssim 1500$ (Duan, Beekman & Martín 2010, 2011), whereas similar values were reached in LES (Stolz & Adams 2003). Although still far from values of technological relevance, and accessible in experiments, the Reynolds numbers here attained are sufficient to start observing large-scale influences on the near-wall region (Schlatter *et al.* 2009).

For the sake of notational clarity, the streamwise, wall-normal and spanwise velocity components will be hereafter also denoted as u, v, w, respectively, and either the Reynolds decomposition ($\varphi = \overline{\varphi} + \varphi'$), or the mass-weighted (Favre) decomposition ($\varphi = \widetilde{\varphi} + \varphi''$, $\widetilde{\varphi} = \overline{\rho\varphi}/\overline{\rho}$), will be used for the generic variable φ. Also, consistent with the classical nomenclature (Pope 2000), we define the inner layer as the region $y/\delta < 0.1$, the outer layer as the region $y^+ > 50$, the viscous sublayer as the region $y^+ < 5$, the buffer layer as the region $5 < y^+ < 30$, and the near-wall layer as the region $y^+ < 50$. Referring to the coherent structures, a notational remark is also necessary. In this paper we call large-scale structures those eddies (the term eddy is used to denote a region where one or more flow variables retain a sufficient degree

of coherence, as quantified through the auto-correlation statistics) which populate the outer layer (and scaling with δ) and small-scale structures those which populate the inner layer (scaling with δ_v). This notation is potentially conflicting with that generally adopted by the turbulence community, whereby the term 'large-scale' is used to denote structures associated with the velocity fields, whereas the term 'small-scale' is used to denote structures associated with the field of the velocity gradient. The confusion is avoided here by using the term 'vortical structures' to refer to structures associated with the velocity gradient field.

When dealing with turbulent eddies, we use the terminology 'attached' and 'detached' to denote eddies whose size is larger and smaller than the wall distance, respectively, following the nomenclature introduced by Jiménez & Hoyas (2008), whereas in the original definition given by Townsend (1976) attached eddies were defined as those whose size is proportional to the wall distance. Attached variables are then designated as those variables which can support attached eddies, whereas detached variables only support detached eddies. This is the case of the wall-normal velocity component, which cannot support attached eddies because of the blocking effect of the wall.

3. Turbulence statistics

The validation of supersonic boundary layer simulations is hampered by the limited availability of experimental data, which are far less abundant than for subsonic flows, and which are affected by significant scatter, mainly related to the greater difficulty in getting accurate measurements in the supersonic regime (Smits & Dussauge 2006). As a consequence, validation of compressible boundary layer DNS data is very often made by comparing with equivalent data obtained in the incompressible regime, assuming that Morkovin's hypothesis (Morkovin 1961) holds. In its basic form, Morkovin's hypothesis amounts to stating that the turbulence time and length scales are not affected by compressibility, whose primary effect is the variation of the mean density and of the thermodynamic properties across the wall layer, which also implies variation of the relevant local Reynolds numbers. Assuming that a constant stress layer exists, and neglecting the contribution of molecular viscosity, it follows that

$$\widetilde{u''v''} \sim \left(\frac{\overline{\rho}_w}{\overline{\rho}}\right) u_\tau^2, \quad \left(\widetilde{u_i''^2}\right)^{1/2} \sim \left(\overline{\rho}_w/\overline{\rho}\right)^{1/2} u_\tau. \tag{3.1}$$

Following the mixing length arguments that lead to the incompressible logarithmic law, one can also argue that in the constant stress layer

$$\tau = -\overline{\rho}\,\widetilde{u''v''} = \overline{\rho}\nu_t \frac{\partial \widetilde{u}}{\partial y} = \overline{\rho}\ell_m^2 \left(\frac{\partial \widetilde{u}}{\partial y}\right)^2 = \overline{\rho}_w u_\tau^2, \tag{3.2}$$

where $\overline{\rho}\nu_t$ is the eddy viscosity, and ℓ_m is the typical size of the stress-bearing eddies. Morkovin's hypothesis implies that, as in the incompressible case, the size of eddies in the overlap layer is proportional to the distance from the wall,

$$\ell_m = ky, \tag{3.3}$$

which leads to a logarithmic law of variation for the effective velocity (van Driest 1951),

$$u_{VD}^+ = \frac{1}{k}\log y^+ + C, \quad \mathrm{d}u_{VD} = (\overline{\rho}/\overline{\rho}_w)^{1/2}\,\mathrm{d}\overline{u}, \tag{3.4}$$

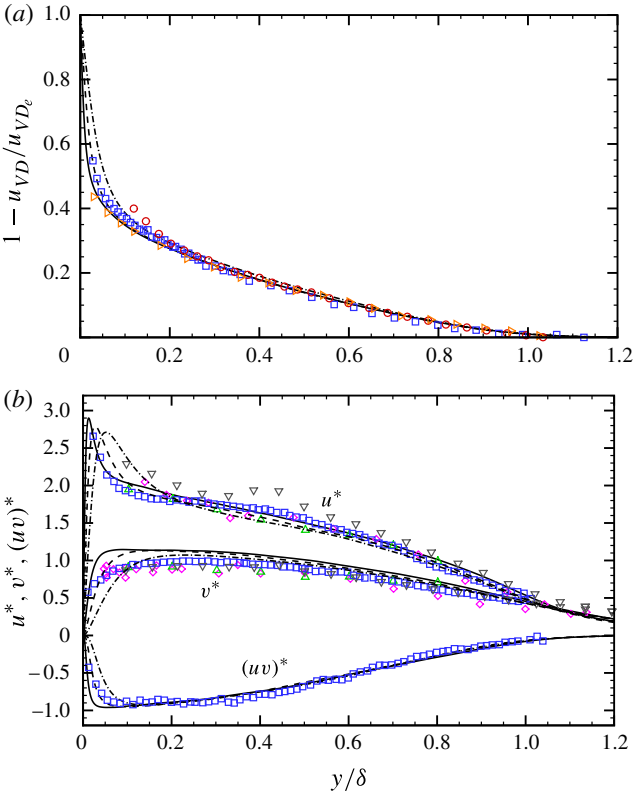

FIGURE 2. (Colour online available at journals.cambridge.org/flm) Comparison of (*a*) van-Driest-transformed mean defect velocity and (*b*) velocity and shear stress fluctuations (the asterisk denotes properties scaled as in (3.1)) with reference experimental data (see table 3 for line legend). Symbols denote experimental data by Eléna & Lacharme (1988) (diamonds), Hou (2003) (down-pointing triangles), Bookey *et al.* (2005) (circles), Humble *et al.* (2009) (up-pointing triangles), Piponniau *et al.* (2009) (squares).

with $y^+ = y/\delta_v$. As pointed out by Smits & Dussauge (2006), the van Driest effective velocity is expected to satisfactorily collapse data in the overlap layer, and (approximately) also in the viscous sublayer, limited to the case of adiabatic walls. The validity of Morkovin's density scaling has been addressed in a series of recent studies (Duan *et al.* 2010, 2011; Lagha *et al.* 2011), which indicate moderate success in scaling mean and fluctuating velocity distributions across a range of Mach numbers, also in the presence of heated and cooled walls. Here we aim at quantitatively establishing the validity of Morkovin's hypothesis in the presence of mild compressibility effects through comparison with state-of-the-art incompressible DNS data at the highest Reynolds numbers currently available.

3.1. *Velocity statistics*

A comparison of the basic velocity statistics with experimental data at similar Mach number (see table 4 for specification of the flow conditions) is shown in figure 2. Given the lack of reliable data in the inner part of supersonic boundary layers and the wide disparity in the Reynolds numbers, the mean defect velocity is reported in outer units in figure 2(*a*), where fair agreement with most experiments is found. Significant

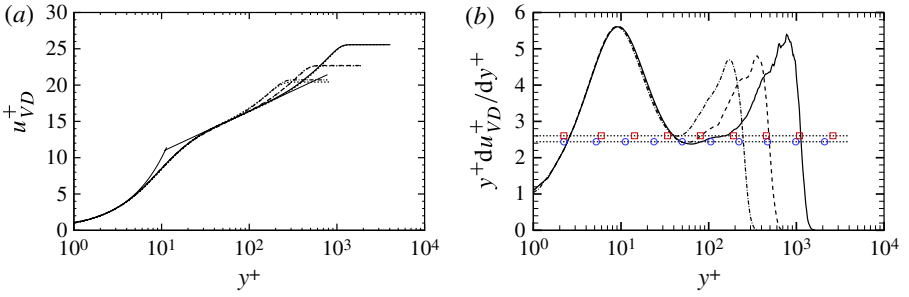

FIGURE 3. (Colour online) Comparison of mean velocity distributions with reference incompressible DNS data (Schlatter & Örlü 2010*a*), shown with dotted lines. The thin solid line in (*a*) denotes the standard law of the wall, compounding $u^+ = y^+$ with $u^+ = y^+/k + C$, $k = 0.41$, $C = 5.2$. (*b*) The compensated mean velocity profiles, the symbols denoting the reference $1/k$ log-law values (circles, $k = 0.41$; squares, $k = 0.384$). See table 3 for line legend.

scatter in the experimental data is observed in the distribution of the turbulence intensities and Reynolds shear stress, shown in figure 2(*b*), where velocity fluctuations are scaled according to (3.1). The figure clearly highlights trends also observed in low-speed boundary layers, on which we will report later on. First, the near-wall peak of the streamwise velocity fluctuations slowly grows with the Reynolds number (by about 7 % in the available range), as a consequence of the increased influence of the large-scale outer-layer structures on the inner-layer dynamics, whereas the opposite behaviour is found away from the wall, the switch between the two behaviours occurring at $y/\delta \approx 0.2$. On the other hand, the wall-normal velocity component and the shear stress seem to consistently asymptote to a limiting plateau distribution, which corresponds to the onset of an equilibrium layer. The DNS results qualitatively agree with all the available experimental data, but much better quantitative correspondence is found with the recent data by Piponniau *et al.* (2009), with the exception of the wall-normal velocity component, which is known to be somewhat underestimated in experiments (Eléna & Lacharme 1988).

A comparison of the velocity statistics with the incompressible dataset of Schlatter & Örlü (2010*a*), here selected for the availability of high-Re data and for the documented absence of post-transitional effects, is displayed in figures 3 and 4. Three stations from Schlatter's dataset have been selected, at which $Re_\tau = 252, 492, 1145$, corresponding to $Re_\theta = 670, 1410, 3630$. These conditions are well suited to compare with the present DNS, being very close in terms of Re_τ (and also in terms of Re_{δ_2}) to the three stations given in table 3.

Figure 3 highlights near collapse of compressible and incompressible DNS data, once density variations are properly accounted for. The agreement also seems to improve as the Reynolds number becomes higher, most likely as a consequence of the onset of clearer separation of scales between the inner and the outer layer, which makes more accurate the hypotheses underlying the derivation of the van Driest velocity scaling. Such nice agreement has several implications. First, it supports the reliability of the present dataset, which, as the reference incompressible data, is apparently free from remnants of the transition process, and therefore can be regarded as an accurate approximation of a fully developed supersonic turbulent boundary layer. Second, to our knowledge, this is the first time that the validity of Morkovin's hypothesis has been so precisely gauged, albeit limited to the weakly

Station #	Dataset	Line type	x_0/δ_{in}	δ/δ_{in}	Re_τ	Re_θ	Re_{δ_2}	H	$C_f(\times 10^3)$	M_τ
1	TBL1	Dot-dashed	87.45	2.75	251	1122	715	3.08	3.19	0.0799
2	TBL2	Dashed	71.64	2.21	497	2377	1516	2.98	2.67	0.0730
3	TBL3	Solid	105.60	2.38	1116	6046	3837	2.91	2.11	0.0649

TABLE 3. Boundary layer properties at the reference streamwise stations considered for the analysis. $C_f = 2\tau_w/(\rho_\infty u_\infty^2)$; $M_\tau = u_\tau/\left(\gamma R\tilde{T}_w\right)^{1/2}$.

	M_∞	Re_τ	Re_θ	Re_{δ_2}	H	$C_f(\times 10^3)$
Eléna & Lacharme (1988)	2.32	1 050	4 700	2 800	3.46	2.15
Smits *et al.* (1989)	2.9	15 000	80 000	39 800	—	2.83
Hou (2003)	2.0	6 758	34 900	23 100	2.89	1.62
Bookey *et al.* (2005)	2.9	501	2 400	1 200	5.49	2.25
Humble *et al.* (2009)	2.1	8 600	49 000	30 500	3.14	1.50
Piponniau *et al.* (2009)	2.28	1 080	5 100	3 100	3.54	2.00

TABLE 4. Summary of parameters for reference supersonic boundary layer experiments.

compressible regime. Third, the results imply that, for many purposes, studies in the mildly supersonic regime directly translate to the incompressible regime.

Besides the favourable agreement with incompressible data, figure 3 highlights several physical features. Upon superficial inspection, figure 3(*a*) seems to support the formation of a logarithmic layer that (at the highest available Re) extends approximately from $y^+ = 50$ to $y^+ = 200$. Inspection of the diagnostic function $y^+ \mathrm{d}u^+_{VD}/\mathrm{d}y^+$, reported in figure 3(*b*) indicates that probably it is not quite the case, since the compensated velocity distribution does not show any significant $1/k$ plateau, at least for $k = 0.41$. However, the formation of an inflection point in the diagnostic function is observed around $y^+ \approx 125$ at the highest Re, for $k \approx 0.384$, which is the asymptotic value suggested for high-Reynolds-number boundary layers (Nagib & Chauhan 2008). Higher Reynolds number data would be needed to confirm or refute this assertion.

Other features are retrieved from inspection of the fluctuating velocity variances, shown in figure 4 in inner scaling. We recall that the attached-eddy hypothesis (Townsend 1976; Jiménez & Hoyas 2008) predicts that the onset of a sensible equilibrium layer is accompanied by the formation of logarithmic layers for the variance of attached variables, whereas no such layer should form for the variance of detached variables. Quantitative predictions for the scaling of the velocity fluctuations based on the attached-eddy hypothesis were made by Perry & Li (1990), who concluded that the variance of the velocity fluctuations should scale as

$$\frac{\overline{u_i'^2}}{u_\tau^2} = B_i - A_i \log(y/\delta) - V(y^+), \tag{3.5}$$

where $B_1 = 2.39$, $A_1 = 1.03$, $B_2 = 1.6$, $B_3 = 1.20$, $A_3 = 0.475$, and $V(y^+)$ accounts for viscous corrections. This inference is essentially confirmed by the data in figure 4(*c*), where the predictions of (3.5) are shown (with $V = 0$) for the streamwise and the

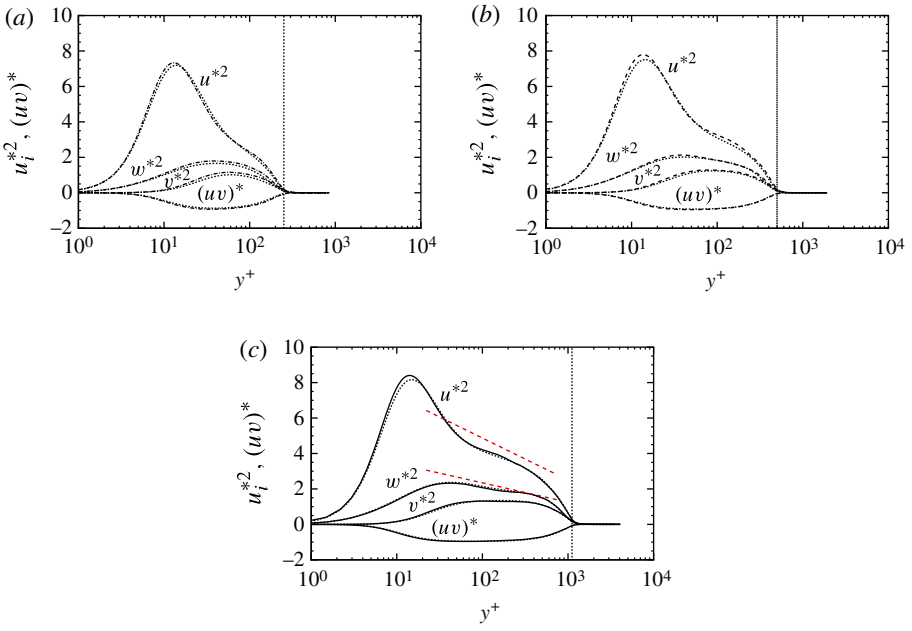

FIGURE 4. (Colour online) Comparison of fluctuating velocity statistics (the asterisk denotes properties scaled as in (3.1)) with reference incompressible DNS data (Schlatter & Örlü 2010*a*), reported with dotted lines. (*a–c*) The distributions of Reynolds stress components at stations 1–3, respectively. Density scaling is used to collapse the two datasets. See table 3 for line legend. The dashed lines in (*c*) correspond to the predictions of (3.5) for $i = 1$ (top), $i = 3$ (bottom). The vertical lines denote the edge of the boundary layer.

spanwise velocity variances. The onset of a logarithmic layer (to be confirmed at higher Re) is noticed, which roughly follows the scaling predicted by (3.5) with $V = 0$, even though the values of B_i seem to be somewhat overestimated. Better approximation of the logarithmic law is seen for the spanwise velocity component than for the streamwise component, which is likely to be contaminated with the peaks caused by the streaks in the buffer layer (Jiménez & Hoyas 2008). One should also note the presence of a bump in the distribution of w' in the outer layer, which is probably the signature of large-scale dynamics in the outer-layer bulges, and which is not present in channel flow DNS (Jiménez & Hoyas 2008).

3.2. *Thermodynamic properties*

Instructive information is gained from inspection of the thermodynamic properties, depicted in figure 5. The thermodynamic fluctuations, especially those of the density field, are useful in turbulence modelling, since they appear in many unclosed terms of the Reynolds-average Navier–Stokes equations, representing the net contribution of mass flux (Gatski & Bonnet 2009). The fluctuating Mach number, reported in figure 5(*a*), is seen to scale well with M_τ. Given the numerical values of the friction Mach number at the three stations here considered (see table 3), it follows that M' is less than about 0.2 throughout the boundary layer. According to the interpretation of Smits & Dussauge (2006), genuine effects of compressibility are then expected to be weak. Figure 5(*b–d*) highlights quite a different behaviour of the fluctuations of density, temperature and pressure. First, it is found that in the viscous and buffer

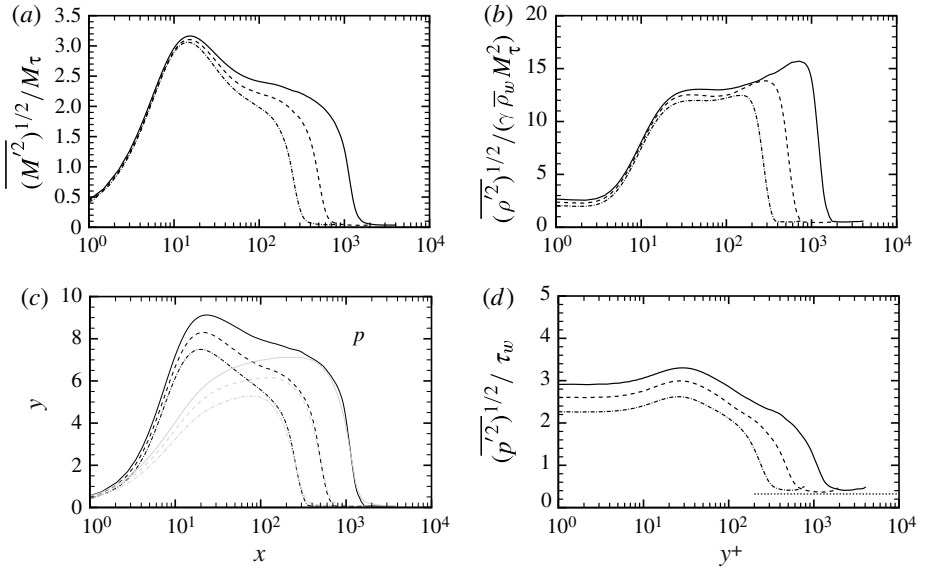

FIGURE 5. Distribution of root-mean-square thermodynamic properties in inner scaling. (*a*) Mach number; (*b*) density; (*c*) temperature and total temperature (grey lines); (*d*) pressure. The horizontal dotted line in (*d*) denotes experimental data taken outside the boundary layer (Laufer 1964). See table 3 for line legend.

layers the pressure and density fluctuations have comparable magnitude, and they are both larger that T'', as a consequence of the isothermal state of the wall. On the other hand, at the edge of the boundary layer, near equilibrium of density and temperature fluctuations is observed, which is indicative of the local importance of the entropic mode, probably associated with sharp gradients of the flow variables at the edge of the turbulent bulges. Outside the boundary layer temperature and density fluctuations become much less than the pressure fluctuations, which is a clear indication of the dominance of the acoustic mode, through which boundary layer noise is radiated to the far field. Incidentally, the observed intensity of the pressure fluctuations is very nearly independent of Re, and close to the experimental correlation data of Laufer (1964) for $M_\infty = 2$ (reported as a dotted line in figure 5*d*). The proposed wall scaling yields good collapse of the temperature and density fluctuations in the inner layer, whereas pressure fluctuations show strong sensitivity to the Reynolds number, which is a hint of strong outer-layer imprinting. A different behaviour of ρ', T'', p' is observed far from the wall, where p' and T'' exhibit a tendency to form logarithmic distributions. Consistent with the previous discussion of Townsend's theory, we may conclude that pressure and temperature are attached variables. Less clear is the behaviour of ρ', which apparently exhibits a plateau in the outer layer. However, as found in the later analysis of the wall imprint of the turbulence eddies, density also has the character of an attached variable. The observed odd scaling can then be explained as a results of the strong peak of density fluctuations at the boundary layer edge.

3.3. *Higher-order statistics*

A comparison of the higher-order velocity statistics with the data of Schlatter & Örlü (2010*a*) is reported in figure 6, where the skewness and the flatness of the streamwise velocity fluctuations are shown, to provide information on the internal intermittency

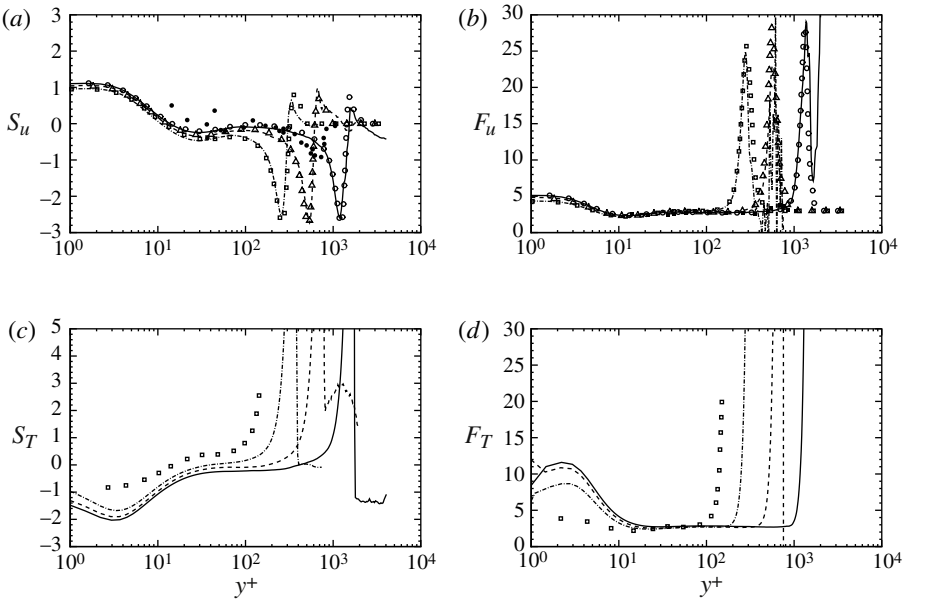

FIGURE 6. Higher-order statistics of streamwise velocity fluctuations (*a*,*b*) and temperature fluctuations (*c*,*d*). The skewness is reported in (*a*,*c*), and the flatness in (*b*,*d*). See table 3 for line legend. In (*a*,*b*) the hollow symbols correspond to the incompressible DNS of Schlatter & Örlü (2010*a*), whereas the filled symbols correspond to the experiments of Eléna & Lacharme (1988). In (*c*,*d*) the symbols correspond to the incompressible DNS data of Kong, Choi & Lee (2000).

of the velocity field. As is well established for canonical channel flows (Kim, Moin & Moser 1987), the probability distribution of the streamwise velocity fluctuations is significantly positively skewed near the wall. Such behaviour is found to be quite insensitive to the Reynolds number, which is an indication of the robustness of the inner cycle of streak formation and bursting (Jiménez & Pinelli 1999). Above the buffer layer the behaviour of turbulence is found to be very nearly Gaussian, with $S_u \approx 0$ (but negative), $F_u \approx 3$, whereas strong intermittency is found again near the edge of the boundary layer, where very large values of the flatness are found. The strongly negative value of the skewness near the edge of the boundary layer suggests the dominance of weak high-speed events, whereas the low-speed events are more intense, but rarer. The distribution of the skewness and flatness of the streamwise velocity nearly superimpose onto the incompressible data of Schlatter & Örlü (2010*a*), also near the edge of the boundary layer, which further indicates that the dynamics of the boundary layer turbulence is essentially incompressible, at least for the flow conditions here considered. Reasonable agreement is also found with internal intermittency measurements available in the supersonic regime (Eléna & Lacharme 1988). Given the similarity of that test case with the present DNS data at station 3, we expect that the mismatch in the position of the boundary layer edge is due to inaccuracy in the estimation of the friction coefficient in the experiments. Also interesting is the distribution of the higher-order statistics of the temperature field, shown in figure 6(*c*) and (*d*), which indicates similar values of the flatness compared to u', but the opposite behaviour in terms of the skewness. As shown later on, this finding is caused by the strong anti-correlation of u' with T'. The trends of

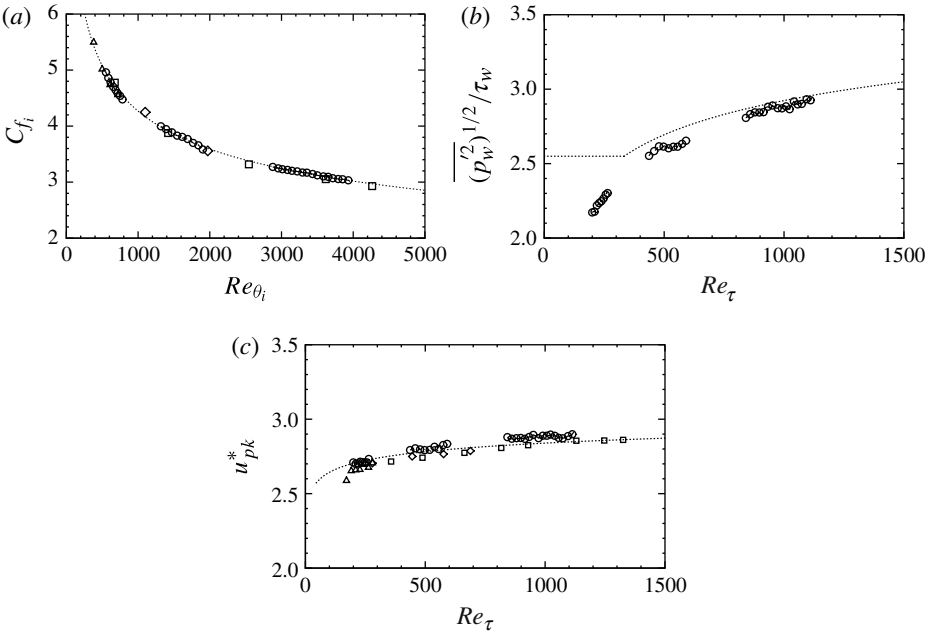

FIGURE 7. Comparison of DNS data with theoretical correlations. Circles denote DNS from TBL1-3 datasets (see line legend in table 4). Other symbols: triangles (Komminao & Skote 2002); squares (Schlatter & Örlü 2010*a*); diamonds (Simens *et al.* 2009). The dotted lines indicate: equation (3.8) in (*a*); (3.9) in (*b*); (3.10) in (*c*).

the skewness and flatness of T' are consistent with those reported by Kong *et al.* (2000) for a heated incompressible boundary layer at $Re_\tau \approx 150$ under isothermal wall conditions, even though the absolute value of the skewness is found to be consistently larger in the present DNS, so is the flatness in the inner layer, which is an indication of stronger intermittency when the temperature field is coupled with the velocity field.

3.4. *Wall properties*

Comparisons of the statistics of wall properties with available correlations are reported in figure 7, which includes the skin friction coefficient (figure 7*a*), the root-mean-square wall pressure fluctuations (figure 7*b*), and the inner-layer peak of the root-mean-square velocity fluctuations (figure 7*c*). Given the scarcity of direct measurements of these properties in the supersonic regime, and/or the problems in obtaining accurate estimates, the DNS data are here compared with existing, well-established incompressible correlations. In this respect we note that, to compare values of the skin friction coefficient at different Mach numbers it is customary to exploit suitable transformations, the best known of which is perhaps the van Driest II transformation (van Driest 1956). As shown by Hopkins & Inouye (1971), this amounts to reducing the friction coefficient and the Reynolds number to 'incompressible' values (denoted with the subscript '*i*'), according to

$$C_{f_i} = F_c\, C_f, \quad Re_{\theta i} = \frac{\mu_\infty}{\overline{\mu}_w} Re_\theta = Re_{\delta_2}, \tag{3.6}$$

where, in the case of an adiabatic wall state

$$F_c = \frac{\overline{T}_w/T_\infty - 1}{\arcsin^2\alpha}, \quad \alpha = \frac{\overline{T}_w/T_\infty - 1}{\sqrt{\overline{T}_w/T_\infty \left(\overline{T}_w/T_\infty - 1\right)}}. \tag{3.7}$$

The transformed skin friction distribution from the present DNS dataset is compared in figure 7(*a*) with selected incompressible DNS data (also reported in the study of Schlatter & Örlü 2010*a*), and with a widely used friction law (Smits, Matheson & Joubert 1983)

$$C_{f_i} = 0.024\, Re_{\theta i}^{-1/4}. \tag{3.8}$$

Excellent collapse on the correlation curve is obtained for all the skin friction data obtained from DNS, which (upon van Driest II scaling) replicate the correct skin friction trend with Re_{δ_2}. This is a further confirmation of the accuracy of the present data, and also of the reliability of the van Driest II transformation in collapsing data at different Mach number. The distribution of the wall pressure fluctuation intensities (scaled by the wall friction) is reported in figure 7(*b*). In the same figure we also show the semi-empirical correlation proposed by Farabee & Casarella (1991),

$$\overline{p_w'^2}/\tau_w^2 = 6.5 + 1.86\, \log(\max(Re_\tau/333, 1)). \tag{3.9}$$

The DNS data show a continuous increase of the inner-scaled pressure fluctuations with Re_τ, at a rate that is consistent with the logarithmic increase of the correlation. This behaviour is likely to be the indication of increased pressure footprint of the outer-layer dynamics (Jiménez *et al.* 2010), which is the subject of a companion study (Bernardini & Pirozzoli 2011*b*). In contradiction of (3.9), the increasing trend is also found to extend to the low-Reynolds-number range. The peak of the streamwise turbulence intensity (shown in figure 7*c*) also consistently increases with Re_τ, highlighting a high-Reynolds-number effect which is well known in the low-speed regime. Overall a trend consistent with the logarithmic law

$$u_{pk}^{*\,2} = 4.837 + 1.075 \log_{10} Re_\tau, \tag{3.10}$$

proposed by Hutchins *et al.* (2009) is observed, even though larger values are observed compared to the incompressible case (also check the u^* peaks in figure 4).

4. Flow organization

The overall organization of the flow can be conveniently investigated by looking at wall-parallel slices, reported in figures 8–10 for the streamwise velocity fluctuations, and in figures 11–13 for the temperature fluctuations field. For the purpose of qualitatively understanding the variation of the typical scales, data are extracted at various distances from the wall. One slice is cut at $y^+ = 15$, which is the location where peak turbulence production occurs, and is representative of the inner-layer turbulence regeneration cycle. One slice is taken at $y/\delta = 0.3$, which is representative of the outer part of the boundary layer, and one at $y/\delta = 0.9$, near the edge of the boundary layer, where the intermittency function (not shown here) attains an inflection point. To rule out any possible artifact associated with the streamwise growth of the boundary layer (Hutchins & Marusic 2007), the slices are extracted by effectively keeping y/δ constant upon interpolation of the numerical data (which are naturally collocated at discrete values of y).

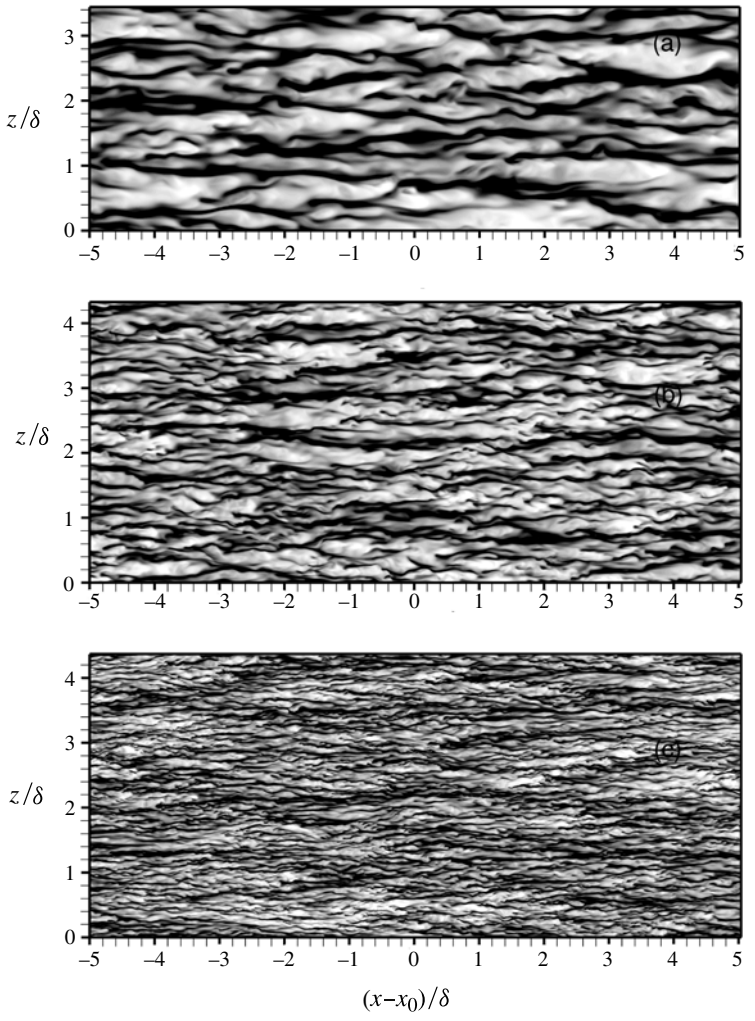

FIGURE 8. Instantaneous streamwise velocity field in the x–z plane at $y^+ = 15$. (*a*) TBL1 ($x_0 = 87.5\delta_{in}$), (*b*) TBL2 ($x_0 = 71.6\delta_{in}$), (*c*) TBL3 ($x_0 = 92.3\delta_{in}$). Contour levels are shown for $-0.25 \leqslant u'/u_\infty \leqslant 0.25$, from dark to light shades.

As seen in figure 8, the velocity field in the inner layer exhibits the typical streaky pattern also observed in low-speed boundary layers, with alternating stripes of enhanced and reduced momentum, which can be interpreted as the remnants of 'sweep' and 'ejection' events, respectively (i.e. wall-ward and outward motions). Similar visualizations of near-wall streaks in compressible boundary layer DNS were also reported by Duan *et al.* (2010, 2011), at $Re_{\delta_2} \approx 1500$. As expected, the typical spanwise size of the velocity streaks in the inner layer is significantly reduced (as a fraction of δ) at higher Reynolds number, scaling in wall units. In the high-Reynolds-number (TBL3) case, besides the obvious fine-scale organization, the near-wall streaks also exhibit distinct larger-scale organization, with apparent clustering of several low- and high-speed stripes, caused by the imprint of overlaying, outer-layer structures (compare with figure 9*c*).

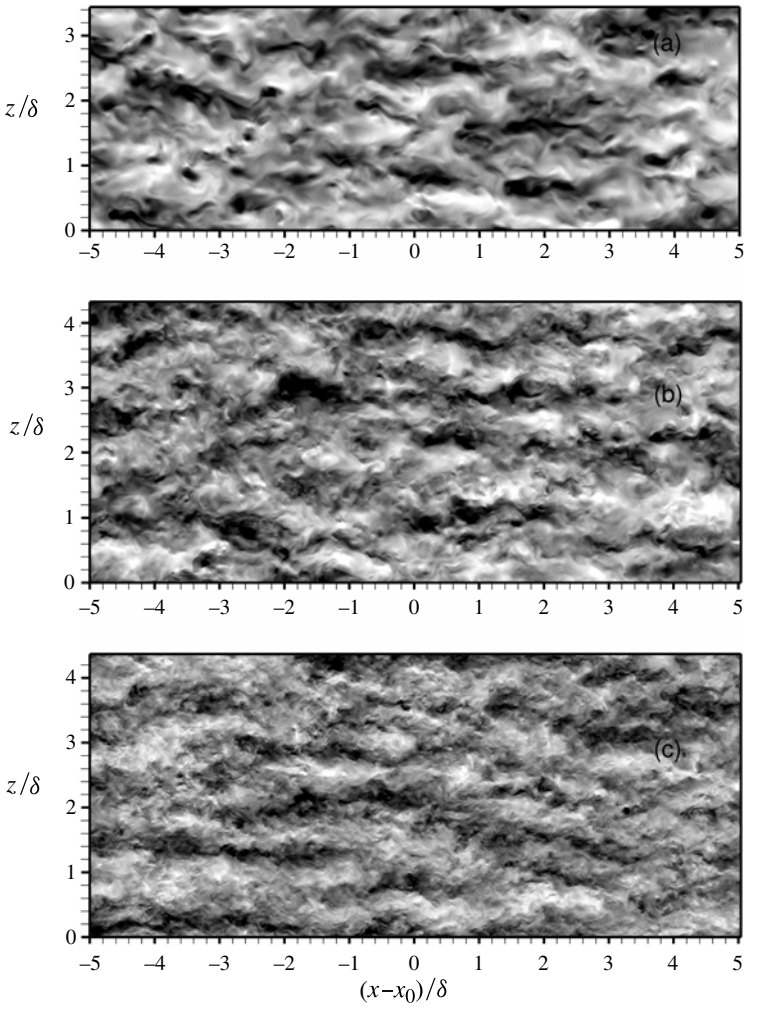

FIGURE 9. Instantaneous streamwise velocity field in the x–z plane at $y/\delta = 0.3$. (*a*) TBL1 ($x_0 = 87.5\delta_{in}$), (*b*) TBL2 ($x_0 = 71.6\delta_{in}$), (*c*) TBL3 ($x_0 = 92.3\delta_{in}$). Contour levels are shown for $-0.15 \leqslant u'/u_\infty \leqslant 0.15$, from dark to light shades.

Looking at the velocity field in the outer layer (figure 9), a qualitatively similar pattern is found at all Re, with high- and low-speed velocity streaks, now on a much larger scale, to which we will refer as outer-layer streaks, and which correspond to the superstructures observed in supersonic experiments (Ganapathisubramani *et al.* 2006). Even though outer-layer streaks have also been observed in DNS at $M_\infty = 3$, Re_τ =300–500 (Ringuette *et al.* 2008), figure 9 clearly shows that they become more and more evident as Re becomes higher, providing evidence for the emergence of substantial energy at low wavenumbers. The spanwise spacing of the outer-layer streaks is found to be of the same order of magnitude for all three simulations, consistent with a change from wall scaling to outer scaling. The scenario changes near the edge of the boundary layer (figure 10), where the flow becomes extremely intermittent, with regions of relatively quiescent, irrotational fluid interspersed with

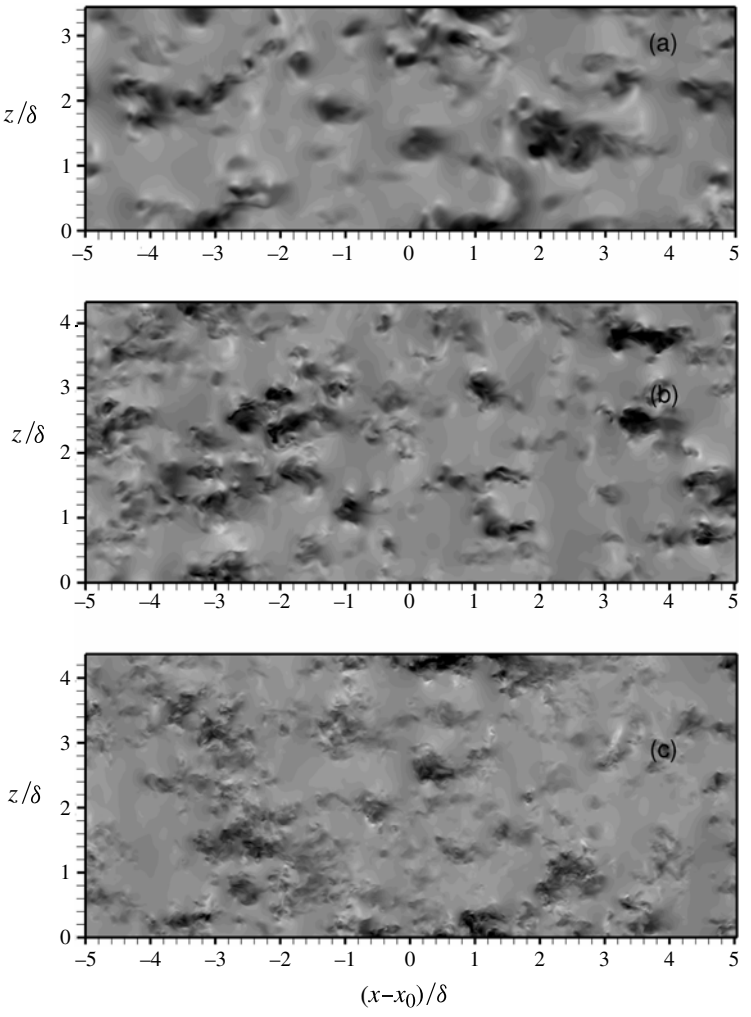

FIGURE 10. Instantaneous streamwise velocity field in the x–z plane at $y/\delta = 0.9$. (*a*) TBL1 ($x_0 = 87.5\delta_{in}$), (*b*) TBL2 ($x_0 = 71.6\delta_{in}$), (*c*) TBL3 ($x_0 = 92.3\delta_{in}$). Contour levels are shown for $-0.12 \leqslant u'/u_\infty \leqslant 0.12$, from dark to light shades.

bulges of rotational fluid erupting from the underlying layers, also apparently scaling with δ.

The temperature field in the inner layer (figure 11) also reveals a clear streaky pattern, qualitatively similar to that of u. Looking carefully, one will observe close correspondence of zones with positive temperature fluctuations with low-speed streaks, and vice-versa. This is a typical manifestation of the well-known tendency for velocity and temperature fluctuations in shear flows to be negatively correlated. In this case, it is an obvious consequence of the fact that the outward wall-normal motions communicate negative velocity fluctuations and positive temperature fluctuations from the inner, low-speed and high-temperature layers, to the upper layers. This behaviour is very similar to that observed in DNS of low-speed thermal boundary layers (Kong *et al.* 2000), and supports a relatively passive role of temperature in the dynamics of supersonic boundary layers (however, recall the observations made regarding the

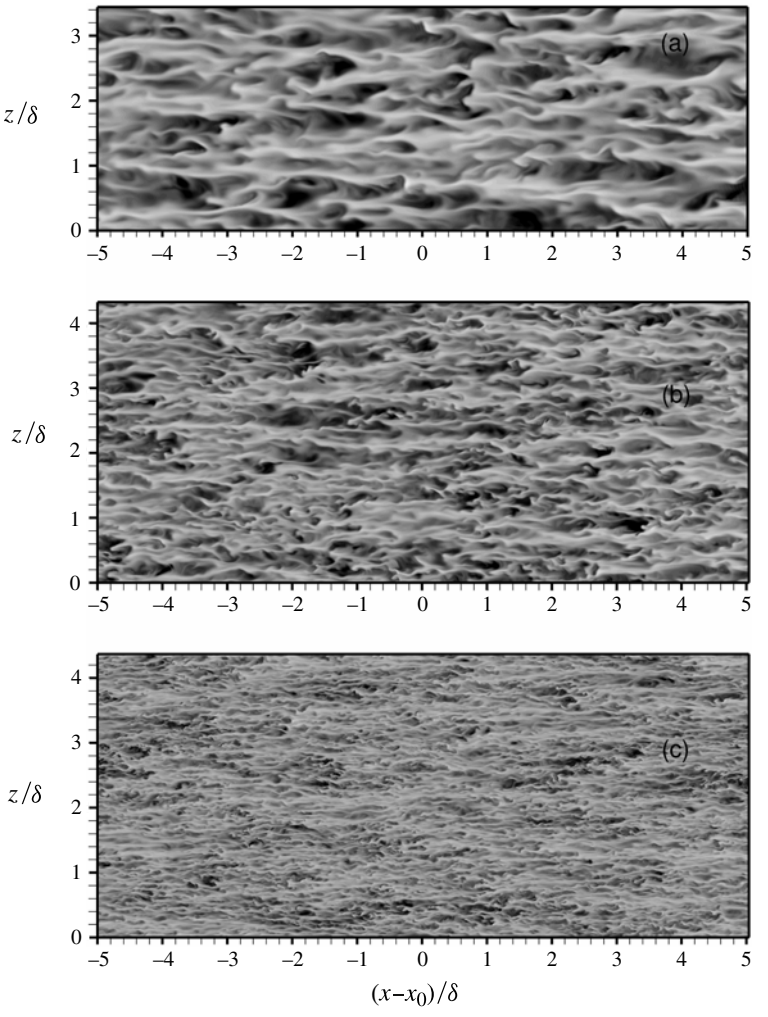

FIGURE 11. Instantaneous temperature field in the x–z plane at $y^+ = 15$. (*a*) TBL1 ($x_0 = 87.5\delta_{in}$), (*b*) TBL2 ($x_0 = 71.6\delta_{in}$), (*c*) TBL3 ($x_0 = 92.3\delta_{in}$). Contour levels are shown for $-0.3 \leqslant T'/T_\infty \leqslant 0.3$, from dark to light shades.

higher-order temperature statistics). Moving to the outer layer the similarity between streamwise velocity and temperature fields becomes less clear, as suggested by comparison of figure 12 with figure 9. Strong correlations of low-speed streaks with negative temperature fluctuations is still observed at this off-wall location. However, the behaviour of temperature fluctuations is here much more 'isotropic' than that of velocity fluctuations, in the sense that the thermal streaks also spread significantly in the spanwise direction. High-temperature streaks tend to manifest themselves with mushroom-shaped heads followed by trailing hot wakes, whereas the low-temperature ones do not seem to have a particular organization. These differences are symptomatic of fundamentally different dynamic behaviour of the temperature and streamwise velocity fields, which apparently were not noticed in previous studies. The temperature field near the edge of the boundary layer (see figure 12) is characterized by mushroom-shaped ejections of fluid erupting into the outer, cooler stream, and which bear

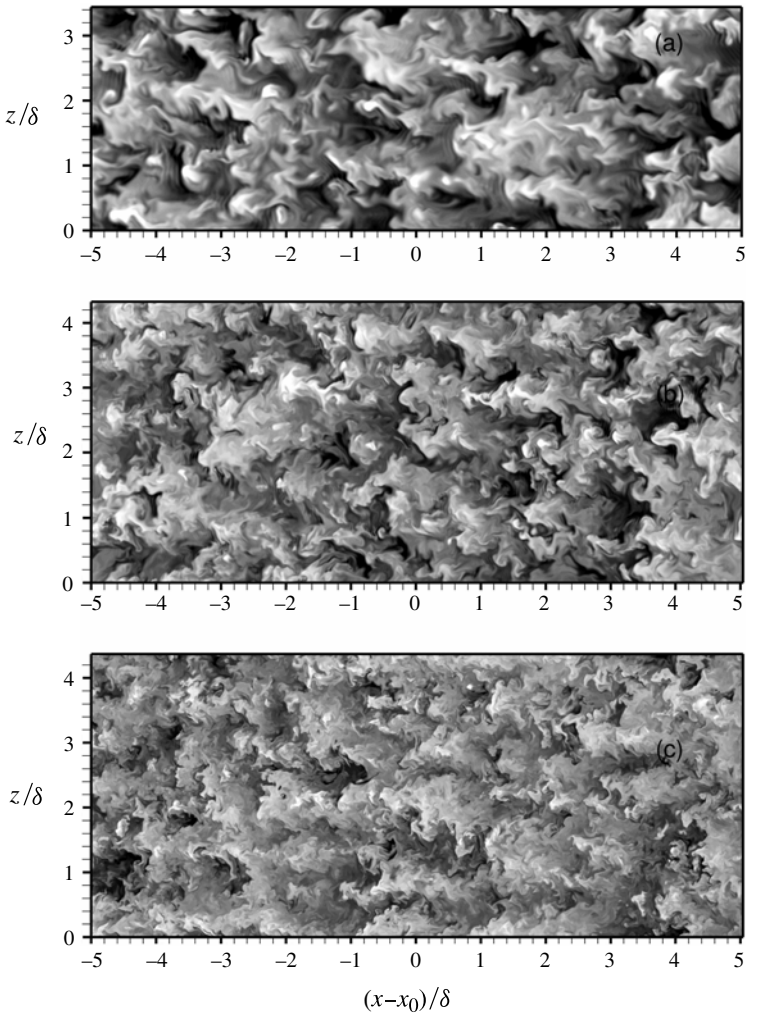

FIGURE 12. Instantaneous temperature field in the x–z plane at $y/\delta = 0.3$. (*a*) TBL1 ($x_0 = 87.5\delta_{in}$), (*b*) TBL2 ($x_0 = 71.6\delta_{in}$), (*c*) TBL3 ($x_0 = 92.3\delta_{in}$). Contour levels are shown for $-0.2 \leqslant T'/T_\infty \leqslant 0.2$, from dark to light shades.

close similarities with the cloud-like structures visualized with the Rayleigh scattering technique (which effectively educes density variations) by Smith & Smits (1995) and Bookey *et al.* (2005). Note that the trailing hot wakes are much shorter at this off-wall location. These observations help to explain the sharp increase of the temperature skewness previously observed in the outermost part of the boundary layers when commenting on figure 6(*c*), which is indicative of very intense events with positive temperature fluctuations (corresponding to hot fluid ejections), whereas low-temperature events are more frequent, but much less intense.

Visualizations of the velocity and temperature fluctuation fields in longitudinal, wall-normal planes are presented in figures 14 and 15. The figures clearly highlight the strongly intermittent nature of the outer-most part of the layer, which is dominated by sharp fronts separating the mainstream irrotational fluid from the inner rotational motions. Such interfaces are rather blurred in the velocity visualizations, whereas

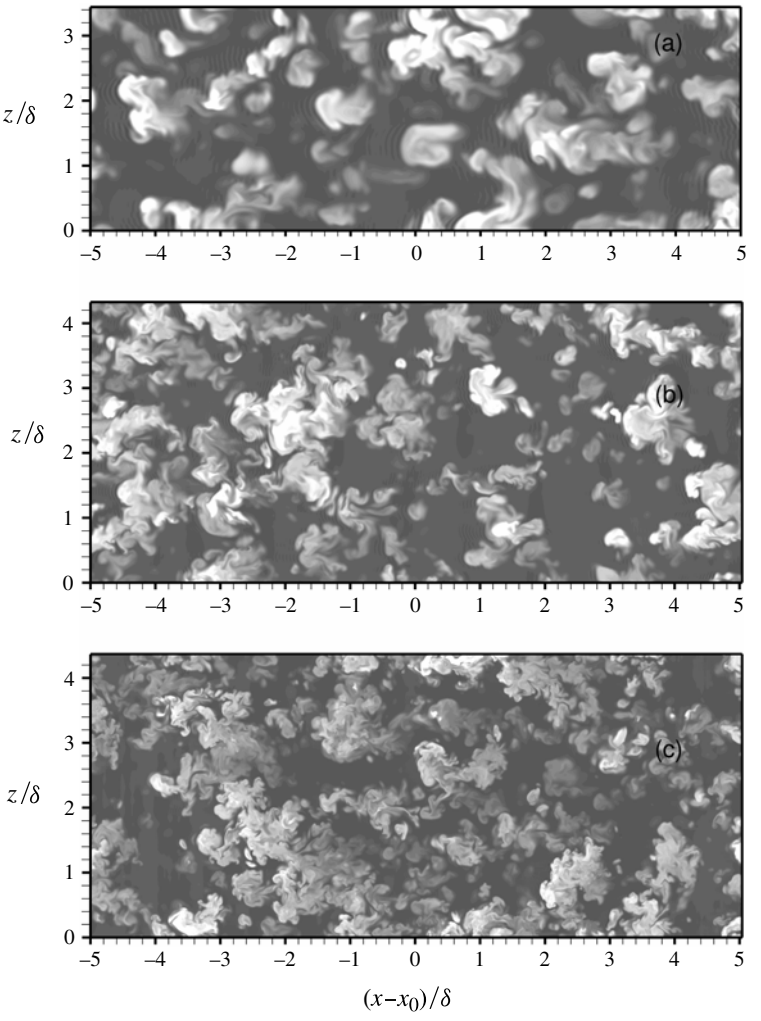

FIGURE 13. Instantaneous temperature field in the x–z plane at $y/\delta = 0.9$. (*a*) TBL1 ($x_0 = 87.5\delta_{in}$), (*b*) TBL2 ($x_0 = 71.6\delta_{in}$), (*c*) TBL3 ($x_0 = 92.3\delta_{in}$). Contour levels are shown for $-0.15 \leqslant T'/T_\infty \leqslant 0.15$, from dark to light shades.

they look much neater in the temperature visualizations. As also found in low-speed boundary layers, deep incursions of outer fluid (valleys) are seen, which reach well into the inner part of the boundary layer. The overall geometry of bulges, as well as their size, is similar at the various Reynolds numbers here considered, which suggests that they obey an outer scaling. As expected, however, finer-scale features are observed at the edge of the turbulent bulges as the Reynolds number increases. A particularly striking feature is the presence (much clearer at higher Re) of large-scale, ramp-shaped zones having relatively uniform momentum (sketched with dashed lines in figure 14*c*), which span the entire boundary layer height, and which were first noticed in the low-speed experiments of Adrian, Meinhart & Tomkins (2000). Those authors reported that the backs of the ramp-shaped structures have typical inclinations of about 12°, which is similar to what is found here. The typical slope of the temperature bulges is apparently much larger, and probably closer to 45° (also see the later

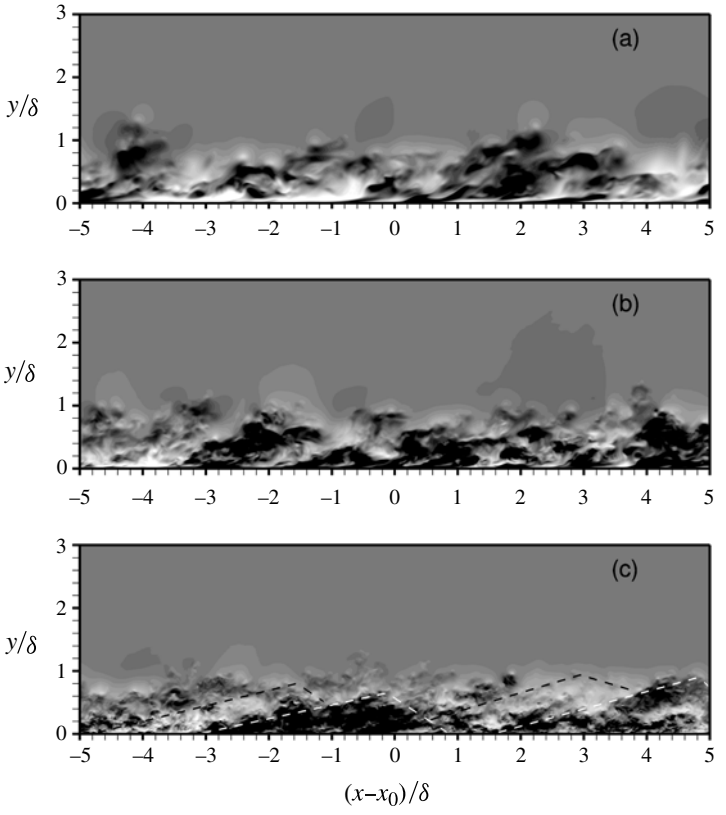

FIGURE 14. Instantaneous streamwise velocity fluctuation field in the x–y plane. (a) TBL1 ($x_0 = 87.5\delta_{in}$), (b) TBL2 ($x_0 = 71.6\delta_{in}$), (c) TBL3 ($x_0 = 92.3\delta_{in}$). Contour levels are shown for $-0.15 \leqslant u'/u_\infty \leqslant 0.15$, from dark to light shades. The dashed lines in (c) highlight tentative boundaries for the large-scale u-bearing eddies.

quantitative analysis). In this respect, we recall that passive scalars in a shearing field are expected to preferentially align in the principal strain direction, which is 45° for a parallel shear flow (Warhaft 2000). A 45° inclination is also frequently quoted in visualization experiments based on passive tracers, and it is the typical inclination of hairpin vortices (Head & Bandyopadhyay 1981). The more shallow angle of the u-bearing eddies compared to the temperature eddies then apparently indicates stronger interaction with the mean flow.

The visualizations in cross-stream planes (figures 16 and 17) help elucidate the scale-separation effect that is typical of higher-Re flows. While the TBL1 dataset does show a single layer of mushroom-shaped eddies which lift momentum and temperature from the wall, the TBL3 dataset clearly highlights the juxtaposition of a population of near-wall eddies resembling those found at low Re_τ, with an additional layer of alternating positive- and negative-velocity eddies, having a roughly circular shape (sketched with dashed lines in figure 16c), and centred at about $y/\delta = 0.3$. We note that a zoom in the near-wall region for the TBL3 dataset (shown in figure 16d of the figures) shows qualitatively the same features as the TBL1 dataset, confirming the invariance of the near-wall motions as Re_τ is increased. Putting these observations together with those made regarding the streamwise and the wall-parallel

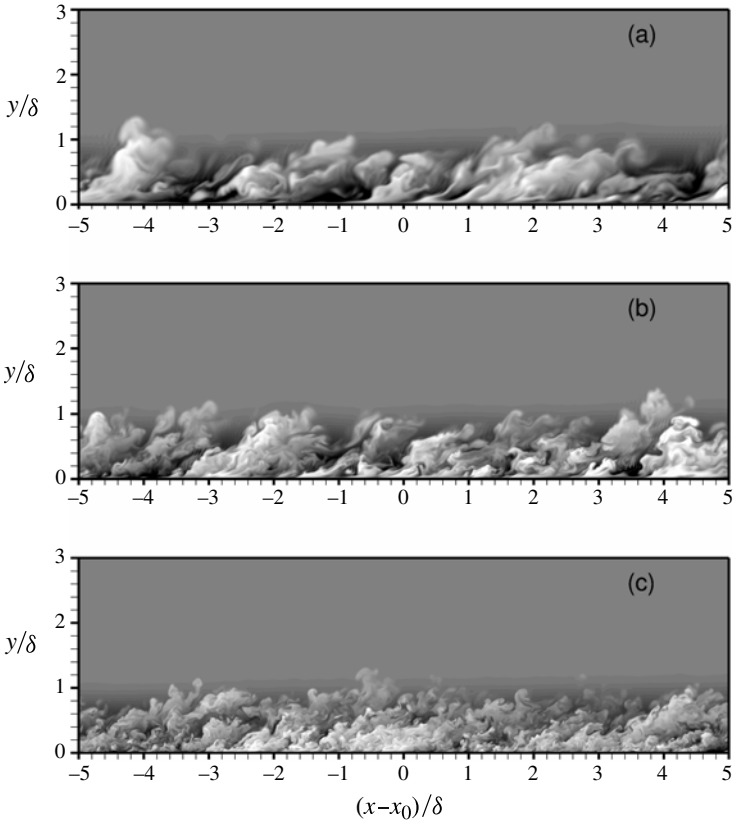

FIGURE 15. Instantaneous temperature fluctuation field in the x–y plane. (*a*) TBL1 ($x_0 = 87.5\delta_{in}$), (*b*) TBL2 ($x_0 = 71.6\delta_{in}$), (*c*) TBL3 ($x_0 = 92.3\delta_{in}$). Contour levels are shown for $-0.2 \leqslant T'/T_\infty \leqslant 0.2$, from dark to light shades.

flow slices one can also conclude that the outer-layer u-bearing eddies that become energetically relevant at high Re_τ have shapes similar to the 'conical eddies' postulated by Townsend (1976), and for which there has been little evidence so far, with the exception of the work of del Álamo *et al.* (2006).

A three-dimensional view of the outer-layer streaks for the TBL3 dataset is given in figure 18, where we report iso-surfaces of negative and positive velocity fluctuations, as well as iso-surfaces of the vortex tube strength (Pirozzoli, Bernardini & Grasso 2010*b*), normalized by the local r.m.s. vorticity (ω'). The figure confirms the hints of two-dimensional representations that the outer-layer structures come in the form of elongated streaks with low and high momentum, the two having similar shapes. The iso-surfaces of the vortex strength indicator highlight the presence of a multitude of small-scale, tube-like structures, very few of which have shapes conforming to canonical hairpins, such as those found in transitional or post-transitional flows (Wu & Moin 2009). Looking carefully at the figure (also see the top projection in the x–z plane, shown in figure 19*a*), one will see that vortex tubes in the outer layer have a clear tendency to cluster above the low-speed streaks, rather than around the high-speed ones. Evidence for clustering of symmetric and asymmetric hairpin-like vortices above low-speed superstructures in supersonic boundary layers was also provided from DNS data at lower Re (Ringuette *et al.* 2008), and from experiments

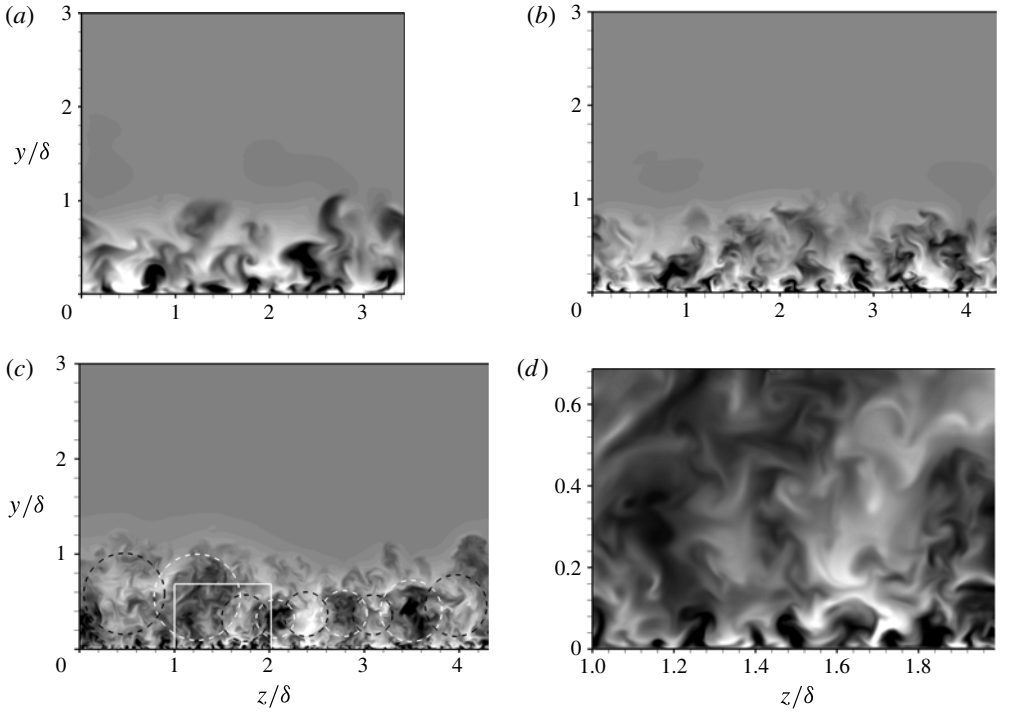

FIGURE 16. Instantaneous streamwise velocity field in the z–y plane. (a) TBL1 ($x_0 = 87.5\delta_{in}$), (b) TBL2 ($x_0 = 71.6\delta_{in}$), (c) TBL3 ($x_0 = 92.3\delta_{in}$). (d) A zoom of the zone marked with a box in (c). Contour levels are shown for $-0.15 \leqslant u'/u_\infty \leqslant 0.15$, from dark to light shades. The dashed circles in (c) highlight tentative boundaries for the large-scale u-bearing eddies.

(Elsinga *et al.* 2010). Inspection of the bottom projection (figure 19*b*) of the flow field highlights vortices residing underneath the outer-layer streaks. In this case, clearer association of clusters of vortex tubes with the high-speed outer-layer streaks is observed.

These findings can be tentatively incorporated into a mechanistic model of outer-layer turbulence by regarding low-speed streaks as wakes, and high-speed streaks as jets, both embedded in a shearing velocity field. As is well known, the outer interfaces of jets and wakes tend to roll up to form compact ring-shaped vortical objects upon Kelvin–Helmholtz instability. The rings, whose axis would be aligned with the streamwise direction, would then undergo the action of shear, giving rise to hairpin-shaped structures (Suponitsky, Cohen & Bar-Yoseph 2005). The sense of the mean shear is such as to promote the (clockwise) vorticity on top of the low-speed streaks, and inhibit the (counter-clockwise) vorticity on top of the high-speed ones, which are depleted with vortex tubes. The same mechanism promotes the (counter-clockwise) vorticity underneath the high-speed streaks, and inhibits the (clockwise) vorticity underneath the low-speed ones, resulting in the pattern observed in figure 19.

5. Statistical properties of turbulent eddies

In this section we address the statistical structural properties of the eddies embedded in the boundary layer through interrogation of the DNS database. Specifically, we aim

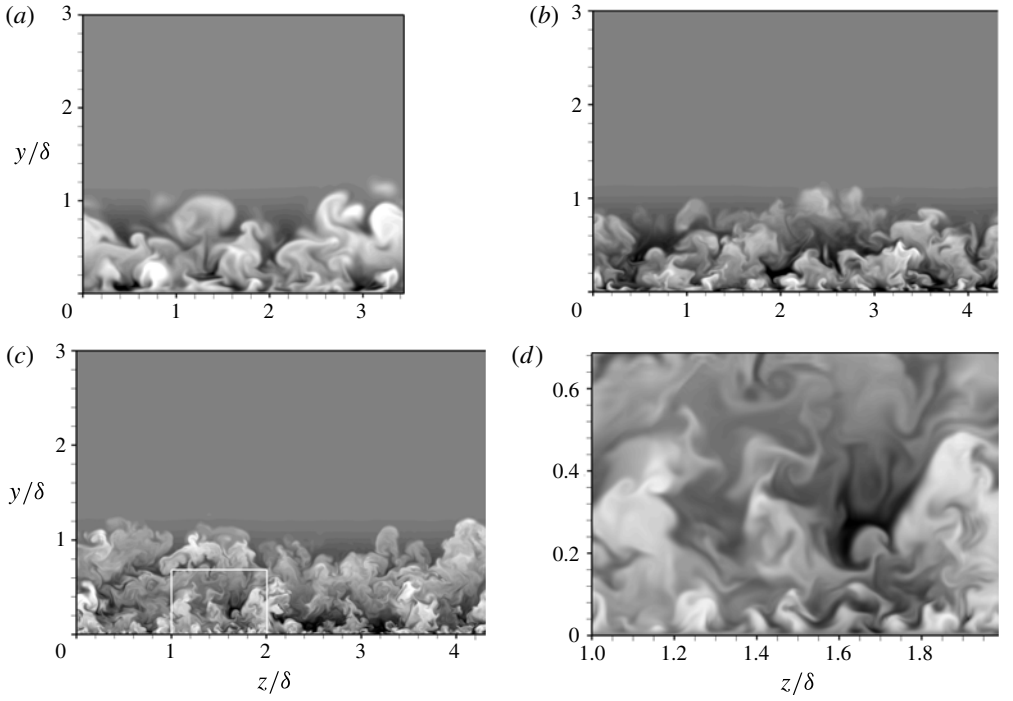

FIGURE 17. Instantaneous temperature field in the z–y plane. (*a*) TBL1 ($x_0 = 87.5\delta_{in}$), (*b*) TBL2 ($x_0 = 71.6\delta_{in}$), (*c*) TBL3 ($x_0 = 92.3\delta_{in}$). (*d*) A zoom of the zone marked with a box in l (*c*). Contour levels are shown for $-0.2 \leqslant T'/T_\infty \leqslant 0.2$, from dark to light shades.

at characterizing the size and the orientation of the typical eddies that populate the wall layer, and elucidate their influence on the boundary layer dynamics. Some of these issues have been partially addressed for incompressible channel flows and boundary layers, but much less is know regarding supersonic boundary layers (Smits & Dussauge 2006).

5.1. *Two-point correlations*

The primary tool to characterize the shape of the turbulent eddies is the two-point autocorrelation, which for the generic variable φ is defined as

$$R_{\varphi\varphi}(\Delta x, y, \Delta z; \bar{y}) = \frac{\langle \varphi(x + \Delta x, y, z + \Delta z, t)\, \varphi(x, \bar{y}, z, t) \rangle}{\langle \varphi^2 (x + \Delta x, y, z, t) \rangle^{1/2} \langle \varphi^2 (x, \bar{y}, z, t) \rangle^{1/2}}, \tag{5.1}$$

the angle brackets denoting averages taken with respect to time, to the spanwise direction, and to the streamwise direction (with the limitations stated in § 2), and $\bar{y}$ representing the wall distance of the point around which the statistics are collected. In figures 20 and 21 the two-point correlations of u', v', T' in the spanwise direction, $R_{\varphi\varphi}(0, y, \Delta z; y)$, are reported at all off-wall distances within the boundary layer. Similar representations were used for channel flows by Jiménez & Hoyas (2008), using the dual spectral representation and taking spectral densities with respect to the streamwise direction. Here we prefer to reason in physical rather than Fourier space, which we believe yields a more direct perception of the structure of the eddies, and mainly consider the correlations in the spanwise direction, since streamwise correlations yield little information on the nature of streaks given their

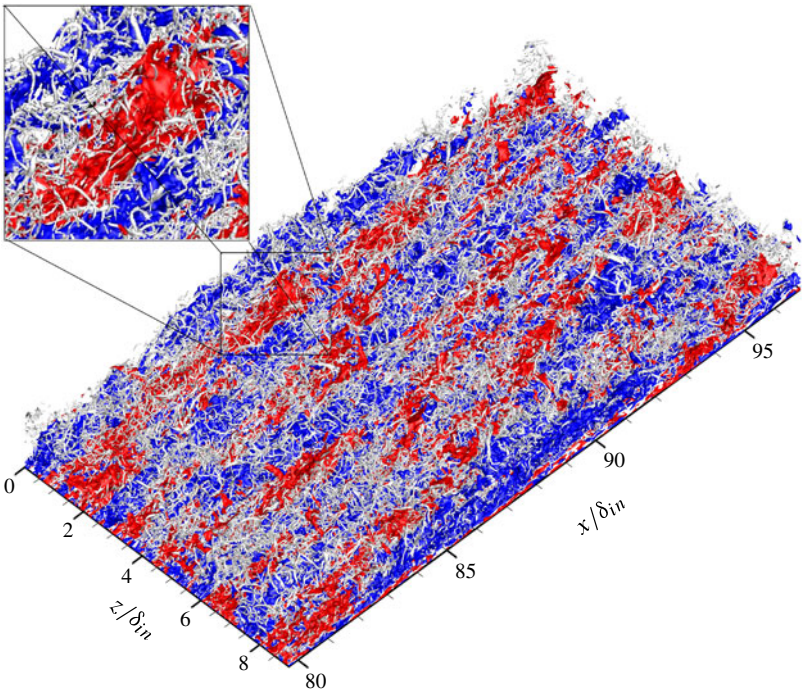

FIGURE 18. Three-dimensional view of outer-layer coherent structures in the TBL3 dataset (only a limited portion of the flow domain is shown). Iso-surfaces of negative velocity fluctuations are rendered in blue ($u'/u_\infty = -0.1$), and positive velocity fluctuations in red ($u'/u_\infty = 0.1$). Iso-surfaces of vortex tubes strength ($\omega_t/\omega_{\rm rms} = 2$) are rendered in grey shades.

peculiar meandering pattern (Hutchins & Marusic 2007). We also note that spectral densities in experiments are usually taken with respect to the streamwise direction by applying Taylor's hypothesis to time series at a given off-wall station, which introduces additional uncertainties (del Álamo & Jiménez 2009).

Inspection of the spanwise u' correlations (reported in figure 20 in both inner and outer units) highlights some fundamental properties of the boundary layer turbulence. First, at least one minimum of the correlation is observed across the boundary layer, whose spanwise distance from the conditioning point generally increases with the wall distance. This is a clear reflection of the streaky pattern of the velocity field, which, as shown in the visualizations of figures 8–10, persists all the way up to the edge of the boundary layer, and whose spacing steadily increases. In the inner layer the first minimum (note that its value becomes positive at higher Re) invariably occurs for spanwise separations $\Delta z^+ \approx 50$, which implies a typical spacing of the streaks $\lambda_z^+ \approx 100$, coincident with the frequently quoted value for canonical low-speed wall-bounded flows (Kim *et al.* 1987). The maximum absolute value of the autocorrelation in the inner layer always occurs at a wall distance $y^+ \approx 15$, which is the signature of the turbulence regeneration cycle (Jiménez & Pinelli 1999). An additional relative minimum is also apparent in the maps in the outer part of the boundary layer, whose position and spanwise separation scales well in outer units, being located at $y = 0.2$–0.3δ, and corresponding to a typical spanwise separation $\Delta z \approx 0.3\delta$. The relative amplitude of the outer-layer minimum becomes significantly stronger than the inner-layer one as Re increases, reflecting the emergence of an outer mode of turbulent

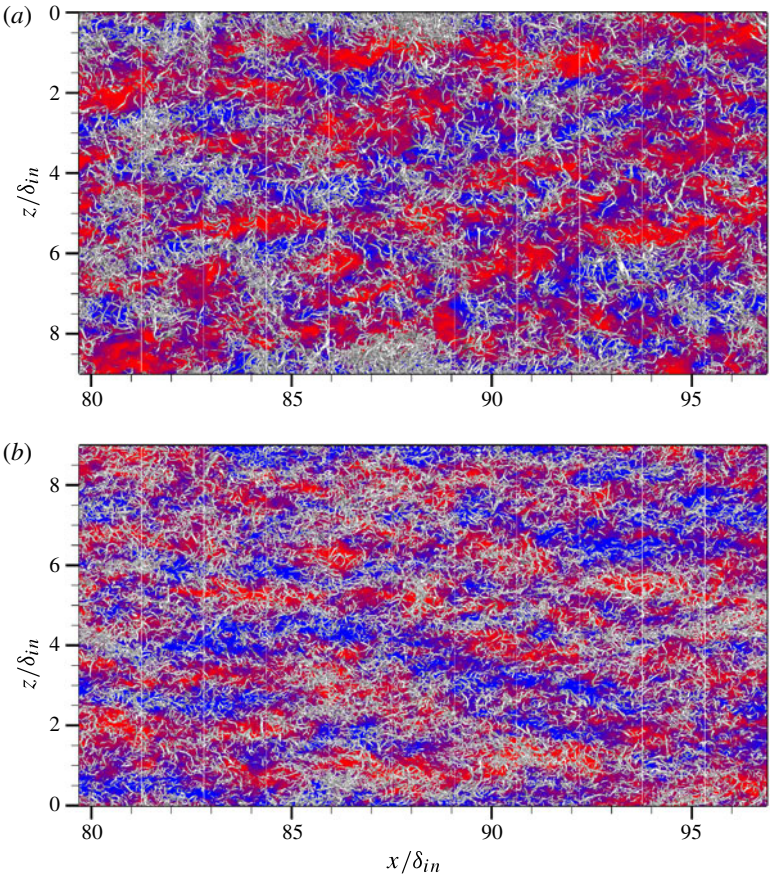

FIGURE 19. Projection of coherent structures in x–z plane, as seen from above (a) and from below (b), for the TBL3 dataset. Flooded contours of u' are shown (contours from $-0.3u_\infty$ to $0.3u_\infty$, blue to red) at $y/\delta = 0.3$, with superposed vortical structures (same as in figure 18).

motion, which was first identified in boundary layers by Hutchins & Marusic (2007), and which was previously noticed in the analysis of the flow visualizations. Given the different scaling of the inner- and outer-layer modes, their positions and scales spread apart as the Reynolds number increases. When scale separation is attained, the outer-layer mode is observed to impose a footprint on the underlying layers through the formation of a large-scale, near-wall minimum. As a consequence, two typical length scales were observed when discussing figure 8(c). In this sense we can affirm that, at sufficiently high Re, the outer-layer eddies that carry streamwise velocity become attached to the wall, their size being at least as large as their distance from the wall. Under these conditions, a logarithmic layer for the variance of u' is expected to form (Townsend 1976), whose onset was observed in figure 4(c).

To get further insight into the change of the typical size of streaks across the boundary layer, in figures 20 and 21 we also report (with dots) iso-lines of multiples of the outer eddy length scale (ℓ_o) defined in (5.4) below, for reasons that will be clarified in the next section. The iso-lines of $\beta\ell_o$ (where β is an arbitrary multiplicative constant) are found to be nearly parallel to the local iso-correlation curves, especially for large values of the correlation. On the other hand, the iso-

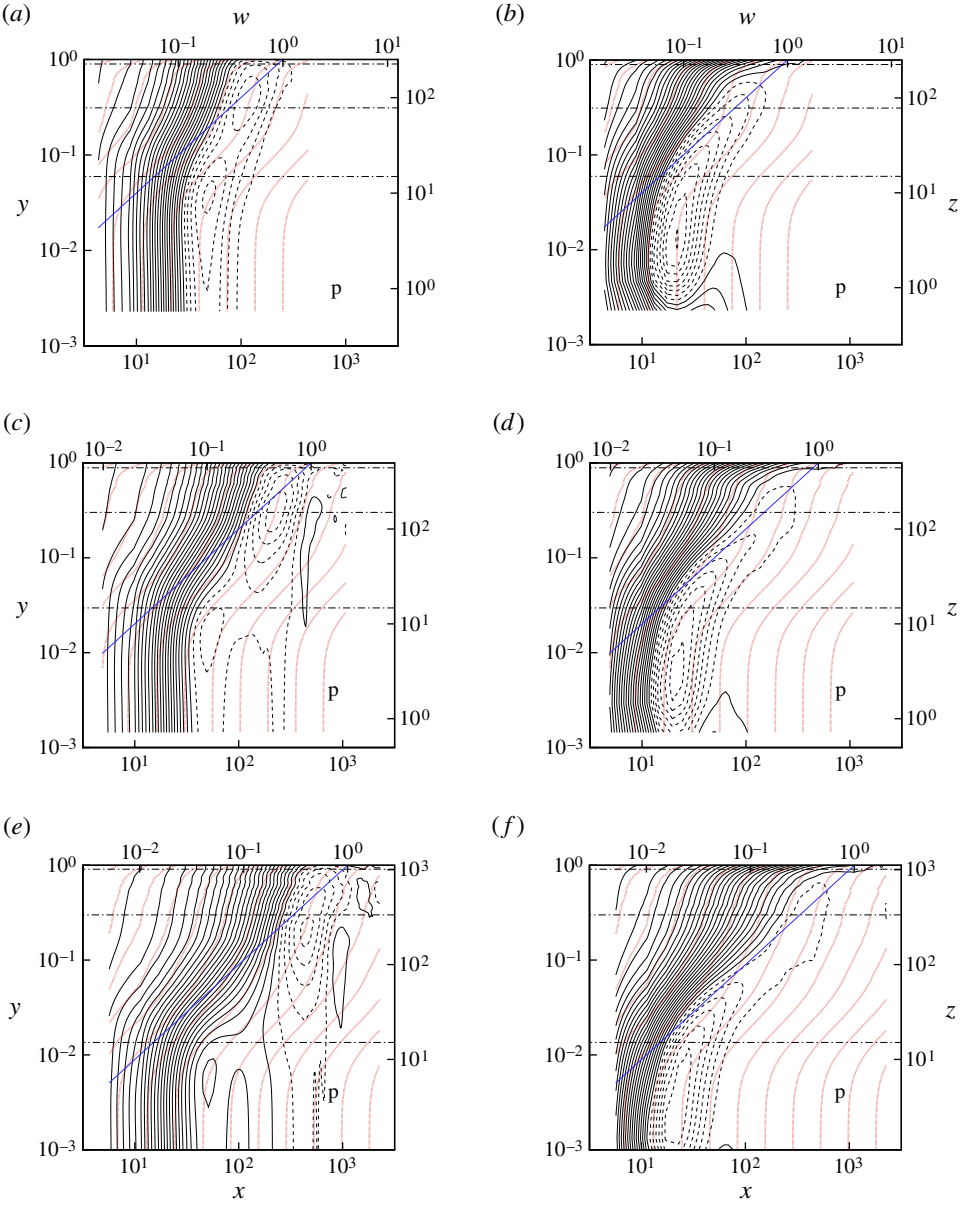

FIGURE 20. (Colour online) Maps of spanwise autocorrelation $R_{\varphi\varphi}(0, y, \Delta z; y)$ of streamwise ($\varphi = u$, left column) and wall-normal ($\varphi = v$, right column) velocity fluctuations. *a,b* TBL1, *c,d* TBL2, *e,f* TBL3. Thirty-two contour levels are shown, from -0.3 to 1 (the dashed pattern denotes negative values). The dotted lines denote iso-lines of $\beta\ell_o$ (see (5.4)), for $0.01 \leqslant \beta \leqslant 10^2$ (sixteen logarithmically spaced contours are shown). The solid diagonal line highlights the trend for 'wall-tangent' eddies ($\Delta z = y$). The horizontal lines indicate the position of representative wall-parallel flow sections ($y^+ = 15$, $y/\delta = 0.3$, $y/\delta = 0.9$).

correlation curves of u' are observed to scale quite poorly with the wall distance (the trend is given by the solid diagonal line $\Delta z = y$).

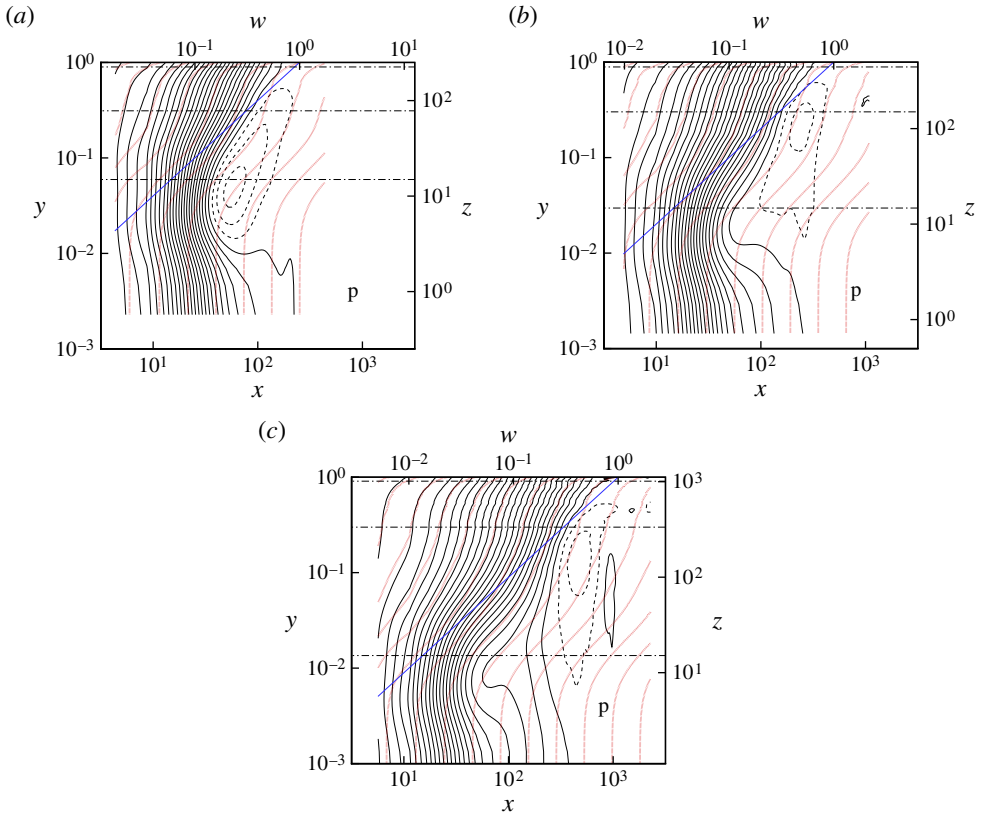

FIGURE 21. (Colour online) Maps of spanwise autocorrelation of temperature fluctuations $R_{TT}(0, y, \Delta z; y)$. *a* TBL1, *b* TBL2, *c* TBL3. Thirty-two contour levels are shown, from -0.3 to 1 (the dashed pattern denotes negative values). The dotted lines denote iso-lines of $\beta\ell_o$ (see (5.4)), for $0.01 \leqslant \beta \leqslant 10^2$ (sixteen logarithmically spaced contours are shown). The solid diagonal line highlights the trend for 'wall-tangent' eddies ($\Delta z = y$). The horizontal lines indicate the position of representative wall-parallel flow sections ($y^+ = 15$, $y/\delta = 0.3$, $y/\delta = 0.9$).

The autocorrelation maps of the wall-normal velocity fluctuations, in the right column of figure 20, show quite a different scenario, and a single negative minimum is observed throughout the boundary layer, whose spanwise separation gradually increases on moving away from the wall. The iso-correlation lines in this case are are found to follow less closely the scaling with ℓ_o, and a narrow region with linear scaling of the v-bearing eddies with the wall distance is perhaps observed in the TBL3 dataset. In the near-wall region the minimum typically occurs at $\Delta z^+ = 25$ which, consistent with the classical interpretation (Kim *et al.* 1987), is the signature of streamwise counter-rotating rollers having a diameter of about 50 wall units. It is important to note that, unlike the streamwise velocity, the behaviour of v' does not significantly change with Re_τ, and no imprint on the near-wall region is observed. Accordingly, v has to be regarded as a detached variable, and accordingly its variance (again recalling figure 4) does not show any tendency to form a logarithmic layer.

The autocorrelations of T', shown in figure 21, exhibit a pattern qualitatively similar to the streamwise velocity, with clear evidence for large-scale organization in the

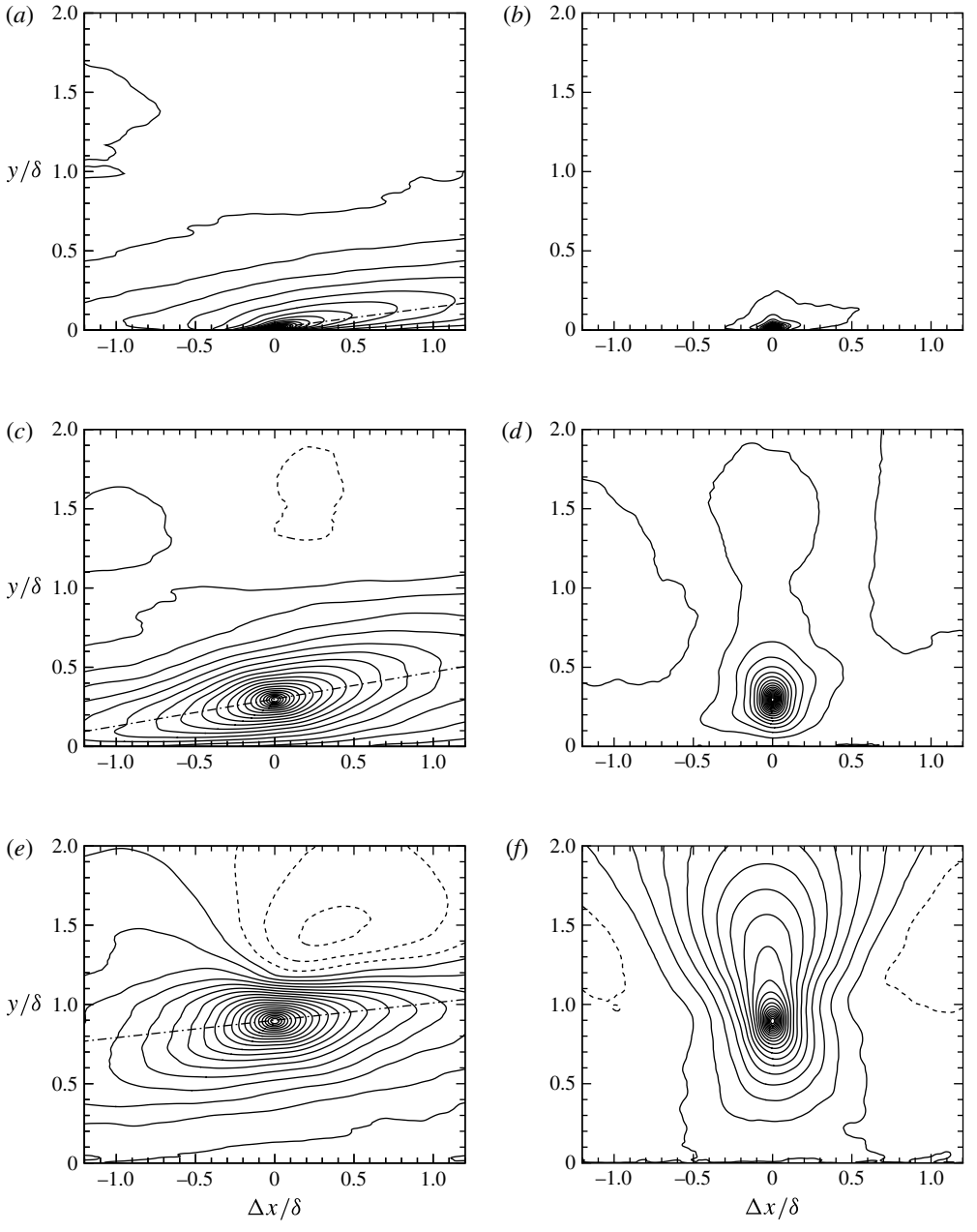

FIGURE 22. Autocorrelation maps ($R_{\varphi\varphi}(\Delta x, y, 0; \overline{y})$) of streamwise (left column) and wall-normal (right column) velocity fluctuations in x–y plane for (a,b) $\overline{y}^+ = 15$, (c,d) $\overline{y}/\delta = 0.3$, ($e$,$f$) $\overline{y}/\delta = 0.9$, for the TBL3 dataset. Levels from -0.2 to 1 are shown, in steps of 0.05. The dot-dashed lines indicate the regression curves obtained from least-square fit of the autocorrelation of u'.

outer layer at high Re_τ, and a negative correlation peak corresponding to thermal streaks which extends all the way down to the buffer layer. However, since the mean temperature gradient goes to zero at the wall (recalling that the wall is nominally

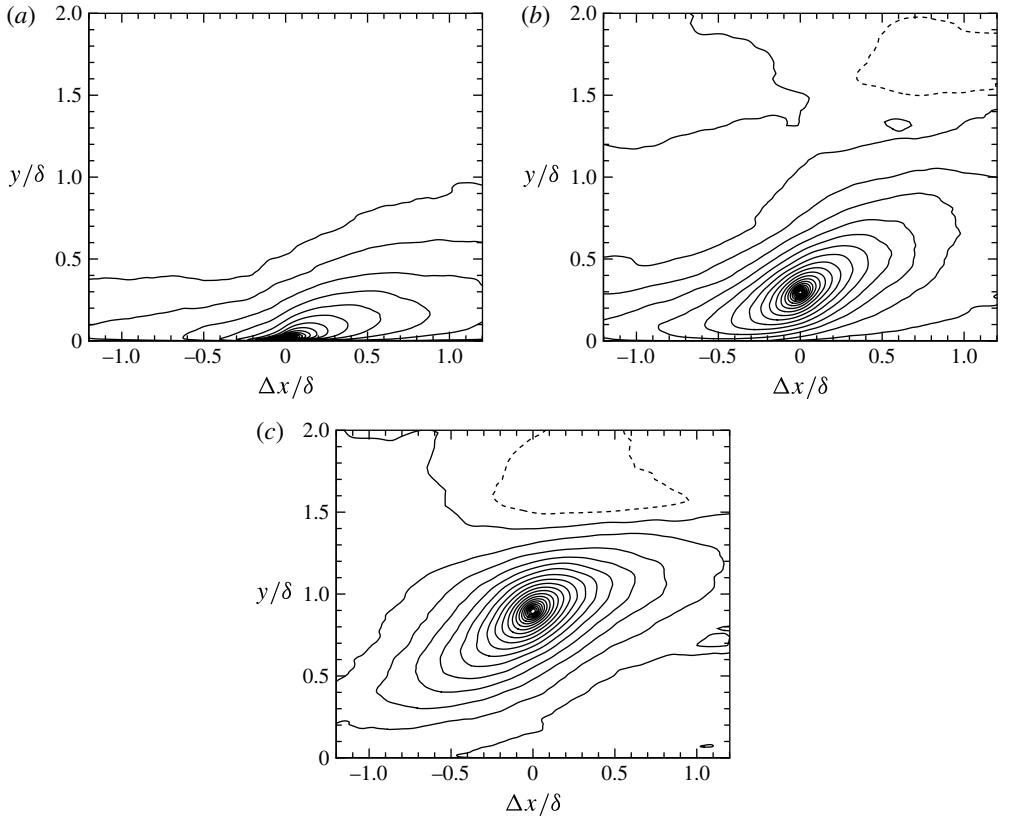

FIGURE 23. Autocorrelation map of temperature fluctuations ($R_{TT}(\Delta x, y, 0; \overline{y})$) in x–y plane for (*a*) $\overline{y}^+ = 15$, (*b*) $\overline{y}/\delta = 0.3$, (*c*) $\overline{y}/\delta = 0.9$, for the TBL3 dataset. Levels from -0.2 to 1 are shown, in steps of 0.05.

adiabatic), the negative peak becomes much weaker, turning into merely a dip in the correlation curve, and vanishing in the viscous sublayer, owing to the absence of significant turbulent transport of temperature. Although the outer T-bearing eddies maintain a footprint in the near-wall region, this is much weaker than for the u-bearing eddies, and their influence apparently does not reach down to the wall. The maps of density, pressure, and spanwise velocity correlations (not reported) also show a characteristic imprinting of the outer-layer eddies on the near-wall region, which supports the wall-attached character of those variables.

Some insight into the orientation of the turbulent eddies can be gained from inspection of the spatial autocorrelations of the flow variables in the x–y plane, $R_{\varphi\varphi}(\Delta x, y, 0; \overline{y})$. The maps corresponding to conditioning events located at $\overline{y}^+ = 15$, $\overline{y}/\delta = 0.3$, $\overline{y}/\delta = 0.9$ are reported in figures 22 and 23, where only the statistics corresponding to the TBL3 dataset are shown, the others being qualitatively similar. In the near-wall region the velocity streaks appear to be lifted away from the wall at a narrow angle, and exhibit streamwise coherence over many δ values. Further away from the wall the correlation also becomes wide in the wall-normal direction, and significant anti-correlation of streamwise velocity disturbances located on opposite sides of the boundary layer edge is observed. The organization of the wall-normal velocity, shown in the right column of figure 22, is quite different, consisting of

compact motions in the near-wall region, and of strongly elongated motions in the wall-normal directions for eddies centred in the outer layer. This scenario is consistent with the observations of Jiménez *et al.* (2010) that 'the structures of u are long, and those of v are tall'. Inspection of the v' autocorrelation in the outer layer for the outermost probing station also highlights the presence of two negative lobes, located right outside the boundary layer on both sides of the primary positive lobe, at about $\pm\delta$. Together with the observations made for u' one can then envisage a scenario whereby an outward ejection (i.e. a strong positive-v' event, with associated negative-u' event) taking place near the boundary layer edge, causes an outward excursion of the turbulent/non-turbulent interface. As a consequence, acceleration of the outer stream takes place, which is highlighted by the negative u' correlation peak in figure 22(c). For continuity, compensating negative-v' events are found on each side of the bulge, whose distance is of the same order of magnitude as the size of bulges visualized in figure 14. The temperature field, whose autocorrelation maps are shown in figure 23, exhibit a pattern very similar to u'. However, at the outer-layer stations the primary correlation ridge seems to be much more inclined with respect to the main stream direction, as a consequence of the more passive dynamics of the temperature field compared to u', and consistent with the steep slope of the temperature fronts seen in figure 15.

5.2. *Structure angles and length scales*

Quantitative information regarding the orientation and the characteristic length scales of the turbulent eddies are collected here, as extracted from the autocorrelation maps. For this purpose, the inclination of the eddies with respect to the streamwise direction is estimated through linear least-square fit of the x–y plane correlations shown in figures 22 and 23. The size of the eddies is instead extracted by considering the integral length scale based on the autocorrelations in the jth coordinate direction,

$$\Lambda_j^{\varphi} = \int R_{\varphi\varphi}(\Delta x_j)\,\mathrm{d}x_j. \tag{5.2}$$

To avoid problems with lack of convergence of the smallest correlation levels, the integration extrema for the evaluation of (5.2) are taken to be the intersections with the $R = 0.05$ correlation iso-level. Marginally different results are obtained with different choices of the threshold level, even though the qualitative trends remain.

Regarding the inclination of the eddies, figure 24 (where only the results for the TBL3 dataset are shown, the others being similar) shows a very different behaviour of the flow variables. As qualitatively observed in figure 22, the u-bearing eddies have shallow angles with respect to the flow direction. In particular, their inclination in the outer part of the boundary layer becomes very close to the 'universal' eddy inclination angle of 14° for the large-scale coherent structures of turbulent boundary layers (Marusic & Heuer 2007), and also to the characteristic 12° inclination angle of the ramp-shaped structures observed by Adrian *et al.* (2000). For comparison, Ringuette *et al.* (2008) report 17°–20° as the typical inclination of vortex packets at $M_\infty = 3$. Since the v-bearing eddies tend to be very elongated in the wall-normal direction, their typical inclination (not reported in the figure) is close to 90°. The ρ-bearing eddies are steeply inclined with respect to the wall, which can be expected given that density (under the assumption of weak compressibility effects) obeys a pure advection equation. The T eddies are typically in between ρ and u, their inclination angle being typically two times larger than that of the u' eddies.

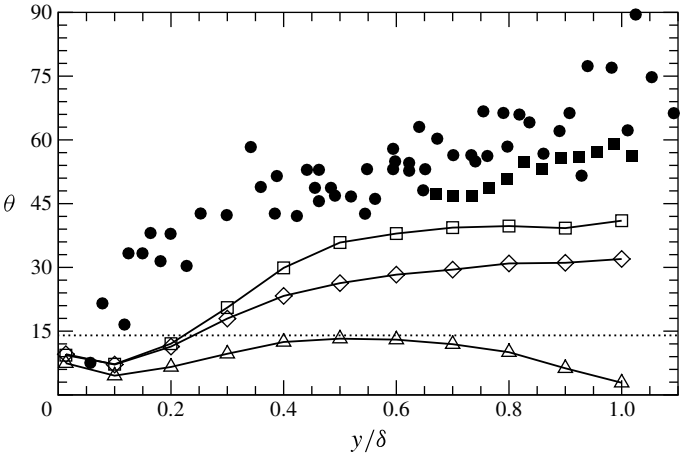

FIGURE 24. Distribution of the 'structure angle' of the flow variables for TBL3 dataset. Symbols: □, ρ; Δ, u; ◇ , T. The horizontal dotted line indicates the typical structure angle (14°) advocated by Marusic & Heuer (2007). Solid circles indicate the structure angle measured from correlations of $(\rho u)'$ by Spina *et al.* (1991), and solid squares denote data from correlations of ρ' by Bookey *et al.* (2005).

We recall that experimental studies in the supersonic regime report typical inclination angles of 30°–60°, based on the analysis of the auto-correlation of the streamwise momentum fluctuations $(\rho u)'$ (Smith & Smits 1995), and of the density fluctuations (Bookey *et al.* 2005). The trends given in those experiments (reported with solid symbols in figure 24) are fully compatible (although the angles are somewhat larger) with those here obtained for the ρ-bearing eddies, but they are certainly much larger than those found for the u-bearing eddies. For consistency with the experiments of Smith & Smits (1995), the size of the (ρu)-bearing eddies was also computed, and found to be very similar to that of the u-bearing eddies. The reason for the lack of agreement with those experiments in not clear at this stage, but part of it might lie (Spina, Donovan & Smits 1991; Smits & Dussauge 2006) in the significant influence of the probe size in the measurement of the two-point correlations in experiments, or to failure of Taylor's hypothesis.

The issue of the typical size of the eddies in wall-bounded flows has been frequently debated both in the incompressible and the compressible flow community. Early experiments (Spina & Smits 1987; Smits *et al.* 1989; Spina *et al.* 1991; Spina, Smits & Robinson 1994) at $M_\infty = 3$ and much higher Re also indicated consistent growth of the (ρu)-bearing eddies with the wall distance, but a strong effect of compressibility was only reported for the streamwise extent, which was found to be reduced by a factor of about two compared to low-speed boundary layers. Recent measurements of correlations in supersonic boundary layers have been performed at $M_\infty = 2$, $Re_\tau = 5600$ by Ganapathisubramani *et al.* (2006), who analysed velocity signals from probes placed in the outer layer, finding an increasing trend with the wall distance of both the streamwise and the spanwise length scales. Quantitative inspection of the correlation maps (see figure 25) indicated strong differences with respect to low-speed measurements, with an increase by a factor of at least four in the streamwise direction and a factor of two in the spanwise direction, which the authors justified by appealing to a wider extension of the logarithmic layer in the supersonic case. Previous DNS data (Duan *et al.* 2011) show very weak compressibility effects on

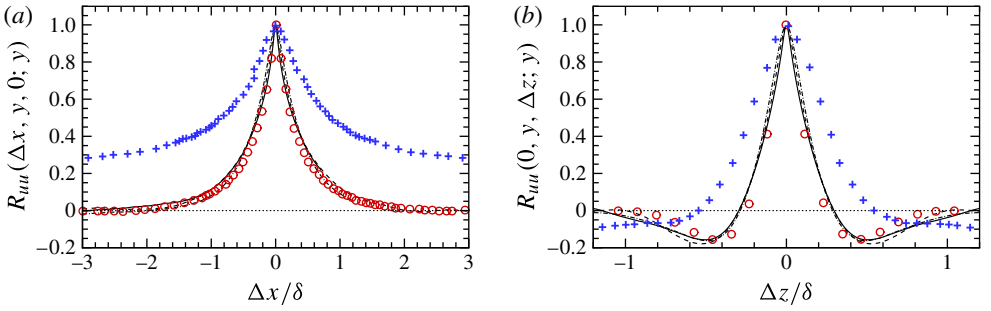

FIGURE 25. (Colour online) Comparison of the streamwise (*a*) and spanwise (*b*) autocorrelation coefficient of u' for $y/\delta = 0.5$, with the experimental data of Hutchins & Marusic (2007) ($M_\infty \approx 0$, $Re_\tau = 1120$, denoted with circles) and of Ganapathisubramani *et al.* (2006) ($M_\infty = 2$, $Re_\tau = 5600$, denoted with crosses).

the size of the eddies up to $M_\infty = 3$, and slow decrease in the streamwise length at higher M_∞.

The computed streamwise and spanwise u' autocorrelations at $y/\delta = 0.5$ are compared with experiments in figure 25. The excellent agreement with the low-speed data of Hutchins & Marusic (2007) at similar Re_τ indicates with little doubt that both the streamwise and the spanwise length scales are weakly affected by compressibility and Reynolds number variation. Looking more carefully one will observe much closer agreement for the streamwise length scale, whereas differences of the order of 15 % are observed for the spanwise length scale. As anticipated, the supersonic experiments of Ganapathisubramani *et al.* (2006) yield much larger correlation length scales, to an extent that is not likely to be explainable by the Reynolds number difference.

The trends of the streamwise and spanwise integral length scales with the wall distance are shown in figure 26 (again, limited to the TBL3 dataset). The streamwise integral length scale of u' (figure 26*a*) shows steady growth in the inner layer, followed by decrease past $y/\delta \approx 0.1$, the typical streamwise length in the outer layer being $\Lambda_z^u \approx 0.8\,\delta$. A very similar behaviour is also found for the temperature field, whose typical length scales are apparently half those for the velocity field. This may be a consequence of the lesser degree of organization of the temperature field in the outer layer (clearly apparent in figure 12). Figure 26 also quantitatively supports the observation that the v-bearing motions are much more compact, having typical length scales of $\Lambda_x^v \approx 0.2\,\delta$ in the outer layer.

As previously pointed out, the trends of the spanwise integral length scales (shown in figure 26 *b*) are more relevant to understand the change of the characteristic size of the eddies across the wall layer, and several low-speed experiments are available for comparison. The data by Monty *et al.* (2007), shown in figure 26(*b*), exhibit the same trend found in the present DNS. Even closer agreement is found by applying the same definition of integral length scale used by those authors (their estimates are based on the distance between two successive $R_{uu} = 0.05$ crossings) to the DNS data, which then yield consistent overprediction of about 15 % with respect to low-speed experiments. The continuous increasing trend of the integral scales of u' with the wall distance was taken by Monty *et al.* (2007) as an indication of the validity of Townsend's attached-eddy hypothesis, whereby the eddy size should scale linearly with the wall distance. In our opinion, based on inspection of figure 26(*b*), no sizeable range with linear variation can be detected, except perhaps for Λ_z^v at $y/\delta \lesssim 0.2$.

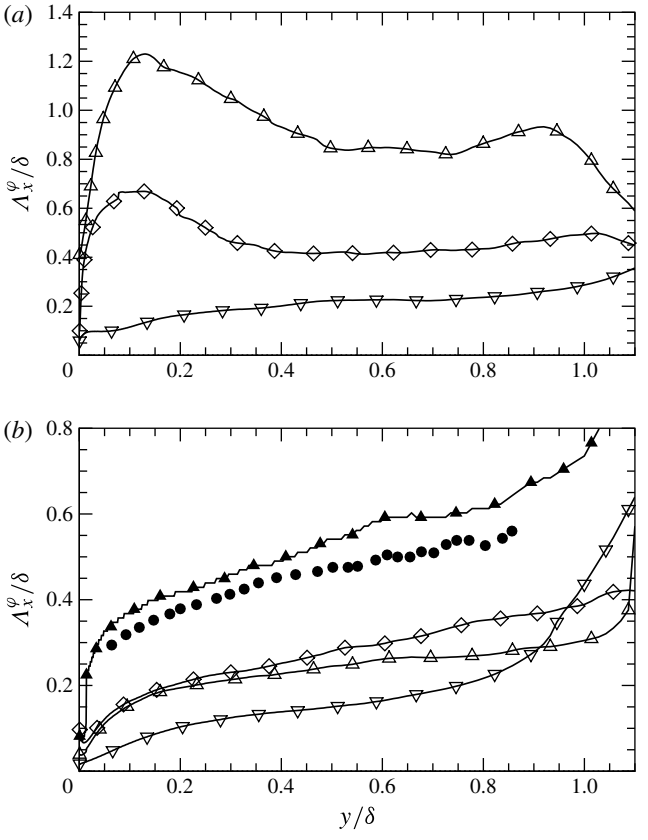

FIGURE 26. Distribution of integral length scales in the streamwise direction (*a*) and in the spanwise direction (*b*) for the TBL3 dataset. Symbols: Δ, $\varphi = u$; ∇, $\varphi = v$; $\diamond$, $\varphi = T$. The filled circles in (*b*) indicate experimental data from Monty *et al.* (2007), and the solid triangles denote the integral length scales of u' determined from the crossing with the $R_{uu} = 0.05$ value.

To explain the observed trends of the eddies size (say, ℓ) we reason that, based on the general assumption that it depends on a typical flow length scale (L), on a typical velocity scale (V), and on the local velocity gradient, and assuming a power-law behaviour, the following scaling results:

$$\frac{\ell}{L} \sim \left(\frac{V}{L}\right)^{\alpha} \left(\frac{\partial \tilde{u}}{\partial y}\right)^{-\alpha}, \tag{5.3}$$

where α is an arbitrary exponent. It is natural to assume that in the inner layer $L = \delta_v$, $V = u_\tau$, and in the outer layer $L = \delta$, $V = u_\tau$, even though some authors would suggest $V = u_\infty$ (George & Castillo 1997). Strict viscous scaling at the wall implies that $\ell \sim \delta_v = \overline{\nu}_w^{1/2} \, (\partial \overline{u}/\partial y)_w^{-1/2}$, whence $\alpha = 1/2$ follows, and the scaling laws for the size of eddies in the outer and in the inner layer become

$$\frac{\ell_o}{\delta} \sim \left(\frac{u_\tau}{\delta}\right)^{1/2} \left(\frac{\partial \tilde{u}}{\partial y}\right)^{-1/2}, \quad \frac{\ell_i}{\delta_v} \sim \left(\frac{u_\tau}{\delta_v}\right)^{1/2} \left(\frac{\partial \tilde{u}}{\partial y}\right)^{-1/2}. \tag{5.4}$$

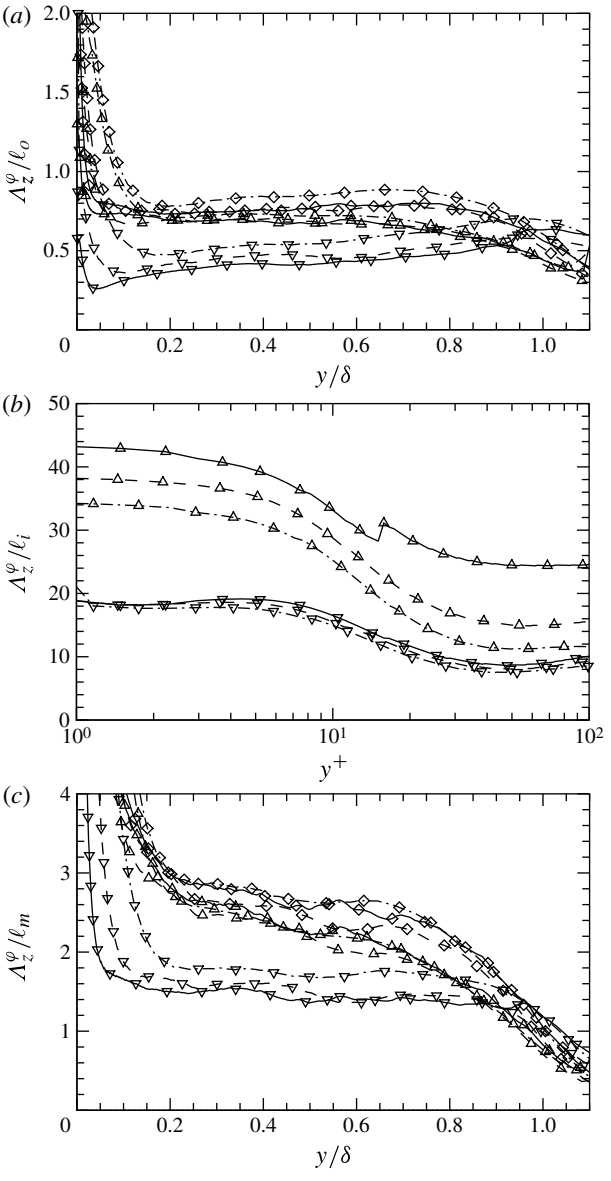

FIGURE 27. Distribution of integral length scales in the spanwise direction, scaled by the reference inner (*a*) and outer (*b*) scales defined in (5.4), and by the local value of the mixing length (*c*) defined in (5.4). See table 3 for line legend. Symbols: Δ, $\varphi = u$; ∇, $\varphi = v$; $\diamond$, $\varphi = T$.

To test the validity of the proposed scalings, in figure 27 the spanwise integral length scales of u', v', T' are scaled with respect to the outer (figure 27*a*) and inner length scales (figure 27*b*) defined in (5.4). It is found that the normalized scales of u' and T' are approximately constant with the wall distance and with Re, which supports a good degree of universality of the proposed scalings. However, a consistent drift to larger values of the inner-layer scales with Re is observed, which is the result of the imprinting of the outer-layer eddies. The proposed scalings apparently do not work

for v', the reason for the failure residing in its nature as a detached variable, which only supports eddies with maximum size equal to the wall distance. Consistently, a nearly linear range of variation of Λ_z^v is observed around $y/\delta \approx 0.1$. An alternative scaling for the eddy size can be considered, based on the mixing length assumption given in (3.2), whereby

$$\ell_m \sim \left(\frac{\tau_w}{\overline{\rho}}\right)^{1/2} \left(\frac{\partial \tilde{u}}{\partial y}\right)^{-1}. \tag{5.5}$$

The integral length scale of the eddies scaled by ℓ_m is shown in figure 27(*c*). This time (paying attention to the range of values in the plots) better collapse of the size of the outer-layer v' eddies is found, compared to the u' eddies. The conclusion might then be drawn that detached eddies approximately scale with the local mixing length, whereas attached eddies scale according to (5.4). Although not shown, the behaviour of the spanwise velocity and of the pressure and density fluctuations also corresponds to that of attached variables.

6. Turbulence modulation

The occurrence of a modulating action of the large-scale outer motions on the small-scale near-wall structures was first investigated in the context of incompressible boundary layers by Mathis *et al.* (2009*a*). Those authors found that, in addition to the (linear) imprinting mechanism previously discussed, nonlinear phenomena of amplitude modulation (AM) also take place between the inner- and the outer-layer eddies. The intensity of the amplitude modulation imparted by a large-scale eddy placed at a location P_1 to a small-scale eddy placed at another location P_2 was quantified by those authors by: (i) determining the high-pass filtered component of the velocity signal at P_2 (say u_{2H}); (ii) demodulating u_{2H} by means of the Hilbert transform to obtain its envelope (say u_{2E}); (iii) determining the low-pass filtered component of the signal envelope (say u_{2EL}); and (iv) calculating the correlation coefficient (hereafter referred to as amplitude modulation coefficient, R_{AM}) between the low-pass filtered envelope at P_2 and the low-pass filtered signal at P_1,

$$R_{AM}^{12} = \frac{\overline{u_{1L}\, u_{2EL}}}{\sqrt{\overline{u_{1L}^2}}\sqrt{\overline{u_{2EL}^2}}}. \tag{6.1}$$

Although the correlation can in general be applied to signals taken from two distinct points, Mathis *et al.* (2009*a*) argued that the one-point AM coefficient provides a reasonable estimate for the full two-point AM coefficient, and exploited a one-point analysis to quantify inner/outer interaction effects across the boundary layer. High levels of positive and negative correlation were observed in the inner and outer region of the wall layer, respectively, with a zero crossing in the logarithmic region. According to the interpretation of Mathis *et al.* (2009*a*), the positive correlation found in the near-wall region indicates that positive (negative) large-scale velocity excursions in the outer layer induce local enhancement (suppression) of the small-scale near-wall turbulent fluctuations. The opposite effect is observed in the outer layer. The analysis was extended to pipe and channel flows by Mathis *et al.* (2009*b*), who observed approximate invariance of the one-point AM coefficient in the inner region when data are compared at similar friction Reynolds number.

The distributions of the computed one-point AM correlation coefficients $R_{AM}^{11}(y)$ (for obvious reasons related to homogeneity of the flow, only the y dependence is left)

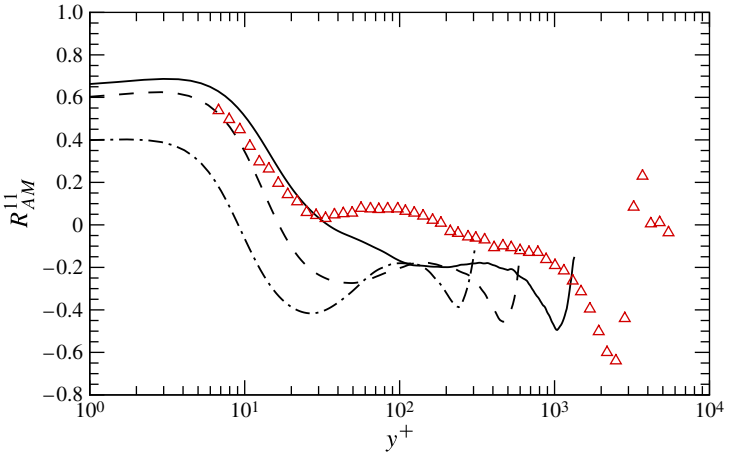

FIGURE 28. (Colour online) Distribution of the one-point amplitude modulation coefficient (R^{11}_{AM}), according to (6.1). The symbols denote experimental incompressible boundary layer data at $Re_\tau = 3020$ (Mathis *et al.* 2009*b*). See table 3 for line legend.

are reported in figure 28, as a function of the wall-normal inner-scaled coordinate. For the purpose of evaluating the various terms in (6.1), filtering is performed in the spanwise direction, with cut-off wavelength $\lambda_z = \delta/2$, which, based on inspection of figure 20, approximately marks the boundary between the small- and the large-scale domains. The effect of varying the filter width was also addressed, but no qualitative change was observed. An overall consistent trend with the experiments of Mathis *et al.* (2009*b*) is found throughout the wall layer, which, in view of the wide disparity in the Reynolds numbers, and of the different approach used for filtering (spatial filtering is used here as opposed to filtering in the time domain in the experiments) makes us confident that the AM quantification procedure is properly implemented. The typical behaviour observed in all canonical wall-bounded flows is recovered, with an inversion of the sign of the modulation coefficient from positive to negative taking place in the DNS data at approximately $y/\delta = 0.035$. The main difference with respect to the experimental measurements resides in the formation of a plateau in the overlap layer, where DNS data level off to about -0.2.

As shown by Schlatter & Örlü (2010*b*), the one-point AM coefficient is strongly related to the local skewness of velocity fluctuations. Indeed, the maps shown in figures 28 and 6(*a*) bear strong similarities. Schlatter & Örlü (2010*b*) were able to show that this similarity also persists when applying the AM analysis to synthetic random signals having the same probability density function as the original velocity signals (and thus having non-zero skewness), indicating an inherent link between skewness and one-point modulation, which does not necessarily reflect genuine physics.

To overcome the possible limitations of the one-point modulation analysis we propose to fully exploit the two-point AM correlation. Specifically, to evaluate the modulation mechanism we consider the two-point covariance between the large-scale velocity at P_1 and the low-pass filtered envelope of the velocity signal at P_2

$$C^{12}_{AM} = \overline{u_{1L}\, u_{2EL}}. \tag{6.2}$$

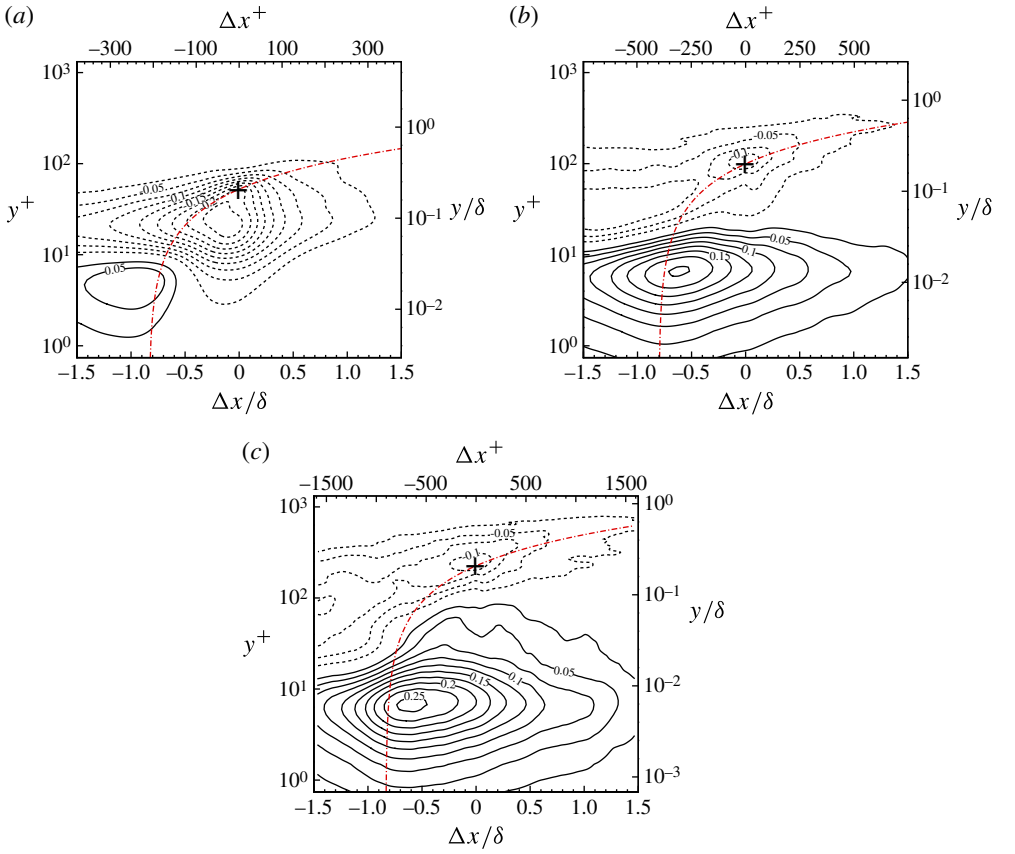

FIGURE 29. (Colour online) Maps of two-point AM covariance (C_{AM}^{12}) of the streamwise velocity, according to (6.2), at (*a*) stations 1, (*b*) 2, and (*c*) 3. The position of the modulating event ($y/\delta = 0.2$) is highlighted with a cross, and data are scaled with respect to u_τ^2. The dot-dashed lines indicate the local 14° direction with respect to the horizontal.

The AM covariance is here preferred over the corresponding correlation coefficient, since it has the advantage of providing a perception of the absolute importance of the modulation effect between any two probe pairs (Bernardini & Pirozzoli 2011*a*). The modulation covariance thus defined is applied to study the modulating influences in the boundary layer by fixing the conditioning point P_1 at $y/\delta = 0.2$, which is representative of the outer-layer eddies. The probe P_2 is then displaced with respect to P_1 in the streamwise and wall-normal directions, thus obtaining AM covariance maps which depend on the wall-normal coordinate and on the streamwise separation, say Δx.

The two-dimensional modulation maps determined from this procedure are shown in figure 29. For clarity of the representation the wall-normal distance is reported in logarithmic scale to zoom into the near-wall region, and the position of the modulating probe is highlighted with a cross. For guidance in the interpretation, the local 14° direction about the modulating point is also drawn with a dot-dashed line. Regardless of Re_τ, a negative modulation peak is observed in the vicinity of the conditioning point, which is associated with the locally negative value of the velocity skewness. More relevant is the emergence of a positive modulation peak in the proximity of the

wall, whose intensity grows at increasing Re_τ, and which is likely to be the signature of a genuine modulating influence of the outer-layer eddies on the near-wall layer. We note that this positive peak approximately leans in the positive 14° direction with respect to the conditioning point, which leads to interpreting the observed positive modulation as the result of the interaction of the large-scale outer-layer u-bearing eddies (statistically embodied by the map of figure 22*b*) with the wall. It is also remarkable that the site where the peak modulation occurs lies, for all cases, at a wall distance $y^+ \approx 6.5$, and its influence extends to both the viscous sublayer and the buffer zone at sufficiently high Re.

7. Thermal statistics

The relationship between velocity and temperature has great relevance in high-speed flight applications, given the strong coupling between thermal heating and the development of boundary layers. A class of useful relations was originally developed by Morkovin (1961), which are collectively referred to as strong Reynolds analogies (SRA), based on the assumption of uniform mean total temperature and negligible total temperature fluctuations (which is clearly violated in the present dataset, see figure 5*c*):

$$R_{uT} = \frac{\widetilde{u''T''}}{\left(\widetilde{u''^2}\right)^{1/2}\left(\widetilde{T''^2}\right)^{1/2}} = -1, \tag{7.1}$$

$$\frac{\left(\widetilde{T''^2}\right)^{1/2}/\tilde{T}}{(\gamma-1)M^2\left(\widetilde{u''^2}\right)^{1/2}/\tilde{u}} = 1, \tag{7.2}$$

$$Pr_t = \frac{\left[-\overline{\rho}\widetilde{u''v''}\right]\partial\tilde{T}/\partial y}{\left[-\overline{\rho}\widetilde{v''T''}\right]\partial\tilde{u}/\partial y} = 1, \tag{7.3}$$

where $M^2 = \tilde{u}^2/(\gamma R\tilde{T})$. Extended versions of the original SRA have been developed by various authors, based on mixing length assumptions, and leading to

$$\frac{\left(\widetilde{T''^2}\right)^{1/2}/\tilde{T}}{(\gamma-1)M^2\left(\widetilde{u''^2}\right)^{1/2}/\tilde{u}} \approx \frac{1}{c\left(1-\partial\tilde{T}_0/\partial\tilde{T}\right)}, \tag{7.4}$$

$$Pr_t = \left(1-\frac{\partial\tilde{T}_0}{\partial\tilde{T}}\right)^{-1} \tag{7.5}$$

where either $c = 1$ (Gaviglio 1987), or $c = Pr_t$ (Huang, Coleman & Bradshaw 1995).

The temperature–velocity correlation and the turbulent Prandtl number obtained from DNS are shown in figure 30. figure 30(*a*) shows lack of correlation between u' and T' in the region immediately adjacent to the wall, where the mean temperature gradient is zero, and therefore turbulent transport of temperature is prevented. The maximum of the correlation coefficient is found in the buffer layer, which becomes weaker with increasing Re. For $y/\delta > 0.5$ the distributions become independent of Re, and level off to about -0.55. A drop in the correlation is observed in the vicinity of the boundary layer edge, a feature which is present in many experiments

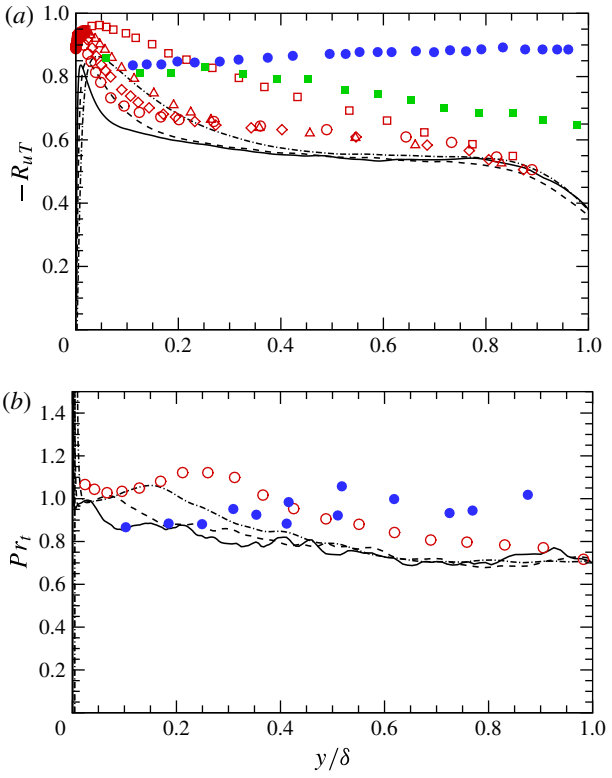

FIGURE 30. (Colour online) Distributions of temperature–velocity correlation coefficient (*a*), and turbulent Prandtl number (*b*). (*a*) The hollow symbols indicate incompressible heated channel flow DNS (Abe & Antonia 2009) at $Re_\tau = 180$ (squares), 395 (triangles), 640 (diamonds), 1020 (circles); solid symbols denote compressible experiments by Debiève (1983) at $M_\infty = 3$, $Re_{\delta_2} = 2720$ (circles) and by Smith & Smits (1993) at $M_\infty = 2.9$, $Re_{\delta_2} = 38\,500$ (squares). (*b*) The hollow symbols indicate incompressible heated boundary layer DNS data by Kong *et al.* (2000), and solid symbols compressible experiments by Debiève (1983).

(including those shown in the figure), but absent from most DNS (with the exception of Guarini *et al.* 2000). The behaviour of R_{uT} (which contradicts (7.1)) reflects the previously noticed association between thermal and momentum streaks within the buffer layer, which becomes weaker in the outer layer. Experimental data in the supersonic regime indicate either a flat (Debiève 1983) or slowly decreasing (Smith & Smits 1993) trend in the outer layer, but with larger absolute values than DNS, and thus in closer agreement with SRA predictions. The turbulent Prandtl number (shown in figure 30*b*) exhibits a near-wall peak in the buffer layer whose strength decreases with Re, and an apparent Reynolds-number-independent decreasing trend for $y/\delta > 0.5$. Also in this case, the basic SRA relation (7.3) is not satisfied, and agreement with supersonic experiments is only fair. Comparison with DNS of incompressible heated wall-bounded flows (Kong *et al.* 2000; Abe & Antonia 2009) shows the same trends as a function of y and Re_τ. However, larger values of R_{uT} and Pr_t are consistently found in that case, which is evidence of stronger dependence of temperature on velocity fluctuations when the former behaves as a passive scalar.

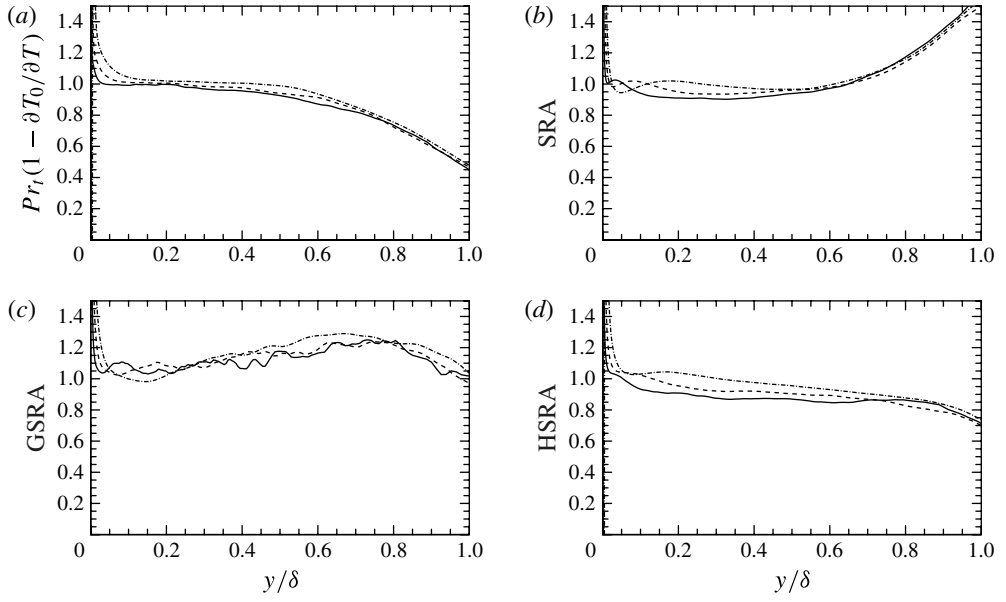

FIGURE 31. Assessment of SRA. (*a*) SRA prediction (7.5) of turbulent Prandtl number. (*b–d*) Predictions of temperature–velocity correlations from SRA: (*b*) Morkovin's analogy (SRA); (*c*) Gaviglio's analogy (GSRA); (*d*) Huang *et al.*'s analogy (HSRA).

An assessment of the various extended SRA relations in the light of the DNS data is attempted in figure 31. To visually appreciate deviations of the DNS data from predictions, the left-hand sides of (7.2), (7.5), (7.4) are divided by the corresponding right-hand sides, so that validity of an SRA relation implies that the associated indicator is unity. figure 31(*a*) shows excellent prediction of the turbulent Prandtl number from the (extended) SRA relation (7.5), and of the temperature–velocity correlation from the standard SRA relation (7.2), for $y/\delta < 0.5$. Even outside that range, the SRA relations satisfactorily remove the Reynolds-number dependence from the data. Better results in the outer layer are obtained with the use of HSRA, for which the indicator function ranges between 0.8 and 1. Overall, the trends are not too far from those seen in the previous study of Guarini *et al.* (2000). We must recall that the present study is limited to a single Mach number, and to adiabatic wall conditions. As shown by Duan *et al.* (2010), the wall thermodynamic state has a strong impact on the performance of SRA. Therefore, it would be interesting to verify the performance of the SRA at high Reynolds numbers in the presence of significant compressibility effects.

8. Conclusions

The structure of supersonic adiabatic boundary layers has been investigated through use of DNS data at $M_\infty = 2$ up to $Re_{\delta_2} \approx 3900$ ($Re_\tau \approx 1120$), which allows one to start probing high-Reynolds-number effects. Particular attention has been paid to the numerical strategy, which apparently does not suffer from problems of spurious numerical dissipation and from artifacts related to improper enforcement of the turbulence inflow conditions. The comparison of the velocity statistics with reference incompressible DNS data shows that (at least at this Mach number) the effects of

the flow compressibility can be effectively incorporated by accounting for the mean density variations across the wall layer. When this is done, the velocity statistics up to fourth order very nearly collapse onto number (either Re_{δ_2} or Re_τ) is matched. To our knowledge, this is the strongest evidence in favour of the validity of Morkovin's hypothesis presented so far. Similarly, extremely precise collapse of the skin friction coefficient onto incompressible scaling laws is observed when the van Driest II transformation is applied, which takes into account density variation effects to leading order. The influence of Reynolds number increase mainly manifests itself by a loss in strict scaling of the near-wall properties with wall units. As also observed in the incompressible regime, the variance of the wall pressure and the squared peak of the streamwise velocity fluctuations are found to grow logarithmically with Re, with weak influence of compressibility.

Flow visualizations have been used to establish the qualitative structure of the inner- and outer-layer eddies, and to quantify their interactions. The nature of the inner-layer energy-containing eddies is found to be the same at all Re, with the typical alternating pattern of high- and low-speed streaks, whose size roughly scales in wall units. A similar pattern (but with length scales comparable to δ) also emerges in the outer layer at sufficiently high Reynolds number, which was not observed in previous numerical simulations. The structures associated with the vorticity field are found to have a typical cane-like shape, and few instances of hairpin-shaped vortices are observed, the boundary layer being fully developed. At high Reynolds number, vortex tubes in the outer layer tend to stand on top of the low-speed streaks, which probably explains why low-speed streaks are more eye-catching compared to high-speed ones. The arrays of vortex tubes 'riding' the low-speed streaks can be identified with the packets of hairpins, that in the commonly accepted view are regarded to be responsible for the formation of superstructures (Adrian *et al.* 2000). On the other hand, it is found that vortices in the inner part of the boundary layer tend to concentrate underneath the outer-layer low-speed streaks. Our interpretation is that vortex tubes (or hairpins) are the consequence, rather than the cause, of the presence of velocity streaks. As discussed in the paper, vortex tubes in the wall layer can be interpreted as the results of the roll-up of vorticity at the edge of the large-scale streaks, under the action of the mean shear. As a consequence of the clockwise orientation of the mean shear, the vortices tend to cluster at the top of the low-speed streaks, and at the bottom of the high-speed ones.

The analysis of the autocorrelations of the flow variables gives quantitative information on the structure of the energy-containing eddies. Some variables, such as u and T, which are 'attached' to the wall, in the sense that they support eddies whose size may be larger than the wall distance, can leave an imprint on the near-wall region. Eddies belonging to this family are found to have size proportional to a length scale based on the local mean shear (in the outer layer, $\ell_o \sim (u_\tau \delta)^{1/2}\ (\partial\tilde{u}/\partial y)^{-1/2}$), and the variance of the associated variables exhibits a logarithmic range of variation in the outer layer. On the other hand, the wall-normal velocity component (which is constrained by the blocking effect of the wall) appears to be detached from the wall, the associated eddies having size which is smaller than the wall-attached eddies, and which approximately scales with the local mixing length scale ($\ell_m \sim (\tau_w/\overline{\rho})^{1/2}\ (\partial\tilde{u}/\partial y)^{-1}$). It should be noted that ℓ_m is bound to vary linearly with the wall distance in the presence of logarithmic variation of $\tilde{u}$, and accordingly a narrow range of linear variation of the size of the v-bearing eddies with the wall distance is found. Given that active motions (i.e. those containing fluctuations of the

wall-normal velocity) are responsible for the production of Reynolds stress, the fact that only the v-bearing eddies scale with the wall distance is entirely consistent with the arguments leading to the logarithmic law for the mean velocity.

Some conclusions can also be drawn regarding the effects of compressibility on the size of the eddies, and specifically of the u-bearing eddies, which have traditionally been studied in experiments. We find that the integral longitudinal length scales are virtually the same as in the incompressible case. Weak effects are discovered on the spanwise length scale, which is found to overestimate incompressible data by 15 % approximately. This contradicts of available experimental data at similar Mach number, which mostly suggest reduction of the longitudinal length scale, and no effect on the spanwise length scale. Exploration of the higher supersonic regime is certainly needed to draw more definite conclusions in this respect. Changes in the typical size of the eddy structures would invalidate the consequences of Morkovin's hypothesis, and thus should be accompanied by sizeable effects on the flow statistics.

Differences are also found in the orientation of the large-scale eddies for the different variables. The u-bearing eddies are found to be typically inclined at 12°–14° with respect to the streamwise direction, which is the same orientation suggested for the large structures in incompressible boundary layers, and which is probably related to the typical inclination of the ramp-like interfaces between zones with different momentum (Adrian *et al.* 2000). Other variables, such as density and temperature, are found to have steeper inclination with respect to the wall, as a consequence of their behaviour being more similar to that of passive scalars, which are expected to align approximately along the 45° direction. The v-bearing eddies have a very different behaviour, being very compact in the wall-parallel directions, and extending their influence mainly in the wall-normal direction.

Besides an imprinting on the near-wall region in the form of juxtaposition of different scales of motion, attached eddies are found to convey a more subtle effect through the modulation imparted to the near-wall small-scale eddies. This effect, which was observed and quantified in low-speed boundary layers, is here characterized in terms of a new metric, namely the amplitude modulation covariance of the velocity field. This tool allows full characterization of the modulating influence of eddies placed in the outer layer (here the reference point is set at $y/\delta = 0.2$) on any other point in the streamwise/wall-normal plane. The main result is the emergence of a positive modulation peak whose amplitude steadily grows with Re, which is approximately oriented in the backward 14° direction with respect to the modulating probe, and which is located at the root of the buffer layer ($y^+ \approx 6.5$). The presence of this peak sheds further light on the previous observation that near-wall vortices are mainly found underneath large-scale high-speed streaks. Indeed, positive values of the modulation indicate that large-scale high-velocity events in the outer layer are associated with increased small-scale activity in the wall proximity. One can then envisage a scenario where local increase of streamwise velocity in an extended region of the outer layer induces local increase of the mean shear, which results in local enhancement of turbulence production near the wall.

Finally, the relationships between temperature and velocity fluctuations have been investigated, and the validity of the set of relations known as SRA has been put to the test. Consistent with the observations of the velocity and temperature fields, the u–T correlation is found to be always negative, with modulus close to unity in the inner layer, and decreasing to about 0.5 in the outer layer as a consequence of the different behaviour of the velocity and temperature streaks. The turbulent Prandtl number if found to be significantly different from unity, contrary to the prediction of

the standard form of the SRA. On the other hand, the modified form of SRA which incorporates the effect of variation of the total temperature is found to better predict the variation of Pr_t, at least up to $y/\delta = 0.5$. In the same region of the wall layer the classical SRA provides good predictions of the temperature variance as a fraction of the velocity variance, whereas modified analogies seem to give uniformly good predictions throughout the boundary layer.

We believe that the present effort constitutes the most complete description of the structure of turbulence at moderately supersonic boundary layers currently available, and the database itself can be usefully exploited for improving and calibrating turbulence models for high-speed, high-Reynolds-number flows. Of course, it needs to be completed with data from simulations at higher Mach number to more completely establish trends related to the effects of compressibility. Work in this direction is in progress.

The statistics of the database presented in the paper are available on-line at the web page http://reynolds.dma.uniroma1.it/dnsm2/, together with supporting documentation.

We acknowledge the Italian computing center CINECA for the availability of high-performance computing resources and support through the 2010/11 ISCRA Award.

REFERENCES

ABE, H. & ANTONIA, R. A. 2009 Near-wall similarity between velocity and scalar fluctuations in a turbulent channel flow. *Phys. Fluids* **21**, 025109.

ADRIAN, R. J., MEINHART, C. D. & TOMKINS, C. D. 2000 Vortex organization in the outer region of the turbulent boundary layer. *J. Fluid Mech.* **422**, 1–54.

DEL ÁLAMO, J. C. & JIMÉNEZ, J. 2009 Estimation of turbulent convection velocities and corrections to Taylor's approximation. *J. Fluid Mech.* **640**, 5–26.

DEL ÁLAMO, J. C., JIMÉNEZ, J., ZANDONADE, P. & MOSER, R. D. 2006 Self-similar vortex clusters in the turbulent logarithmic region. *J. Fluid Mech.* **561**, 329–358.

BERNARDINI, M. & PIROZZOLI, S. 2011*a* Inner/outer layer interactions in turbulent boundary layers: a refined measure for the large-scale amplitude modulation mechanism. *Phys. Fluids* **23**, 061701.

BERNARDINI, M. & PIROZZOLI, S. 2011*b* Wall pressure fluctuations beneath supersonic turbulent boundary layers. *Phys. Fluids* **23**, 085102.

BERNARDINI, M., PIROZZOLI, S. & GRASSO, F. 2011 The wall pressure signature of transonic shock/boundary layer interaction. *J. Fluid Mech.* **671**, 288–312.

BOOKEY, P., WYCKHAM, C., SMITS, A. J. & MARTÍN, M. P. 2005 New experimental data of STBLI at DNS/LES accessible Reynolds numbers. *AIAA Paper* 2005-309.

DEBIÈVE, J. F. 1983 Étude d'une interaction turbulence/onde de choc. PhD thesis, Université d'Aix-Marseille II.

VAN DRIEST, E. R. 1951 Turbulent boundary layer in compressible fluids. *J. Aero. Sci.* **18**, 145–160.

VAN DRIEST, E. R. 1956 The problem of aerodynamic heating. *Aeronaut. Engng Rev.* **15**, 26–41.

DUAN, L., BEEKMAN, I. & MARTÍN, M. P. 2010 Direct numerical simulation of hypersonic turbulent boundary layers. Part 2. Effect of wall temperature. *J. Fluid Mech.* **655**, 419–445.

DUAN, L., BEEKMAN, I. & MARTÍN, M. P. 2011 Direct numerical simulation of hypersonic turbulent boundary layers. Part 3. Effect of Mach number. *J. Fluid Mech.* **672**, 245–267.

ELÉNA, M. & LACHARME, J. 1988 Experimental study of a supersonic turbulent boundary layer using a laser doppler anemometer. *J. Méc. Théor. Appl.* **7**, 175–190.

ELSINGA, G. E., ADRIAN, R. J., VAN OUDHEUSDEN, B. W. & SCARANO, F. 2010 Three-dimensional vortex organization in a high-Reynolds-number supersonic turbulent boundary layer. *J. Fluid Mech.* **644**, 35–50.

ERM, L. P. & JOUBERT, J. 1991 Low Reynolds number turbulent boundary layers. *J. Fluid Mech.* **230**, 1–44.

FARABEE, T. & CASARELLA, M. J. 1991 Spectral features of wall pressure fluctuations beneath turbulent boundary layers. *Phys. Fluids* **3** (10), 2410–2420.

FERNHOLZ, H. H. & FINLEY, P. J. 1976 A critical compilation of compressible turbulent boundary layer data. *AGARDograph* 223.

GANAPATHISUBRAMANI, B., CLEMENS, N. T. & DOLLING, D. S. 2006 Large-scale motions in a supersonic turbulent boundary layer. *J. Fluid Mech.* **556**, 271–282.

GATSKI, T. B. & BONNET, J.-P. 2009 *Compressibility, Turbulence and High Speed Flow*. Elsevier.

GAVIGLIO, J. 1987 Reynolds analogies and experimental study of heat transfer in the supersonic boundary layer. *Intl J. Heat Mass Transfer* **30**, 911–926.

GEORGE, W. K. & CASTILLO, L. 1997 Zero-pressure-gradient turbulent boundary layer. *Appl. Mech. Rev.* **50**, 689–729.

GUARINI, S. E., MOSER, R. D., SHARIFF, K. & WRAY, A. 2000 Direct numerical simulation of a supersonic boundary layer at Mach 2.5. *J. Fluid Mech.* **414**, 1–33.

HEAD, M. & BANDYOPADHYAY, P. 1981 New aspects of turbulent boundary-layer structure. *J. Fluid Mech.* **107**, 297–338.

HOPKINS, E. J. & INOUYE, M. 1971 An evaluation of theories for predicting turbulent skin friction and heat tranfer on flat plates at supersonic and hypersonic Mach numbers. *AIAA J.* **9**, 993–1003.

HOU, Y. X. 2003 Particle image velocimetry study of shock induced turbulent boundary layer separation. PhD thesis, Department of Aerospace Engineering and Engineering Mechanics, University of Texas at Austin.

HOYAS, S. & JIMÉNEZ, J. 2006 Scaling of velocity fluctuations in turbulent channels up to $Re_\tau = 2003$. *Phys. Fluids* **18**, 011702.

HUANG, P. G., COLEMAN, G. N. & BRADSHAW, P. 1995 Compressible turbulent channel flows: DNS results and modelling. *J. Fluid Mech.* **305**, 185–218.

HUMBLE, R. A., ELSINGA, G. E., SCARANO, F. & VAN OUDHEUSDEN, B. W. 2009 Three-dimensional instantaneous structure of a shock wave/turbulent boundary layer interaction. *J. Fluid Mech.* **622**, 33–62.

HUTCHINS, N. & MARUSIC, I. 2007 Evidence of very long meandering features in the logarithmic region of turbulent boundary layers. *J. Fluid Mech.* **579**, 1–28.

HUTCHINS, N., NICKELS, T. B., MARUSIC, I. & CHONG, M. S. 2009 Hot-wire spatial resolution issues in wall-bounded turbulence. *J. Fluid Mech.* **635**, 103–136.

JIMÉNEZ, J. & HOYAS, S. 2008 Turbulent fluctuations above the buffer layer of wall-bounded flows. *J. Fluid Mech.* **611**, 215–236.

JIMÉNEZ, J., HOYAS, S., SIMENS, M. P. & MIZUNO, Y. 2010 Turbulent boundary layers and channels at moderate Reynolds numbers. *J. Fluid Mech.* **657**, 336–360.

JIMÉNEZ, J. & PINELLI, A. 1999 The autonomous cycle of near–wall turbulence. *J. Fluid Mech.* **389**, 335–359.

KENNEDY, C. A. & GRUBER, A. 2008 Reduced aliasing formulations of the convective terms within the Navier–Stokes equations. *J. Comput. Phys.* **227**, 1676–1700.

KIM, J., MOIN, P. & MOSER, R. D. 1987 Turbulence statistics in fully developed channel flow at low Reynolds number. *J. Fluid Mech.* **177**, 133–166.

KOMMINAO, J. & SKOTE, M. 2002 Reynolds stress budgets in Couette and boundary layer flows. *Flow Turbul. Combust.* **68**, 167–192.

KONG, H., CHOI, H. & LEE, J. S. 2000 Direct numerical simulation of turbulent thermal boundary layers. *Phys. Fluids* **10**, 85–91.

LAGHA, M., KIM, J., ELDREDGE, J. D. & ZHONG, X. 2011 A numerical study of compressible turbulent boundary layers. *Phys. Fluids* **23**, 015106.

LAUFER, J. 1964 Some statistical properties of the pressure field radiated by a turbulent boundary layer. *Phys. Fluids* **7**, 1191–1197.

MAEDER, T., ADAMS, N. A. & KLEISER, L. 2001 Direct simulation of turbulent supersonic boundary layers by an extended temporal approach. *J. Fluid Mech.* **429**, 187–216.

MARTÍN, M. P. 2007 Direct numerical simulation of hypersonic turbulent boundary layers. Part 1. Initialization and comparison with experiments. *J. Fluid Mech.* **570**, 347–364.

MARUSIC, I. & HEUER, W. D. C. 2007 Reynolds number invariance of the structure inclination angle in wall turbulence. *Phys. Rev. Lett.* **99**, 114504.

MATHIS, R., HUTCHINS, N. & MARUSIC, I. 2009*a* Large-scale amplitude modulation of the small-scale structures in turbulent boundary layers. *J. Fluid Mech.* **628**, 311–337.

MATHIS, R., MONTY, J. P., HUTCHINS, N. & MARUSIC, I. 2009*b* Comparison of large-scale amplitude modulation in turbulent boundary layers, pipes, and channel flows. *Phys. Fluids* **21**, 111703.

MONTY, J. P., STEWART, J. A., WILLIAMS, R. C. & CHONG, M. S. 2007 Large-scale features in turbulent pipe and channel flows. *J. Fluid Mech.* **589**, 147–156.

MORKOVIN, M. V. 1961 Effects of compressibility on turbulent flows. In *Mécanique de la Turbulence*, pp. 367–380. A. Favre.

NAGIB, H. M. & CHAUHAN, K. A. 2008 Variations of von kármán coefficient in canonical flows. *Phys. Fluids* **20**, 101518.

PERRY, A. E. & LI, J. D. 1990 Experimental support for the attached-eddy hypothesis in zero-pressure-gradient turbulent boundary layers. *J. Fluid Mech.* **218**, 405–438.

PIPONNIAU, S., DUSSAUGE, J.-P., DEBIÈVE, J. F. & DUPONT, P. 2009 A simple model for low-frequency unsteadiness in shock-induced separation. *J. Fluid Mech.* **629**, 87–108.

PIROZZOLI, S. 2010 Generalized conservative approximations of split convective derivative operators. *J. Comput. Phys.* **229**, 7180–7190.

PIROZZOLI, S., BERNARDINI, M. & GRASSO, F. 2010*a* Direct numerical simulation of transonic shock/boundary layer interaction under conditions of incipient separation. *J. Fluid Mech.* **657**, 361–393.

PIROZZOLI, S., BERNARDINI, M. & GRASSO, F. 2010*b* On the dynamical relevance of coherent vortical structures in turbulent boundary layers. *J. Fluid Mech.* **648**, 325–349.

PIROZZOLI, S., GRASSO, F. & GATSKI, T. B. 2004 Direct numerical simulation and analysis of a spatially evolving supersonic turbulent boundary layer at $M = 2.25$. *Phys. Fluids* **16** (3), 530–545.

POINSOT, T. S. & LELE, S. K. 1992 Boundary conditions for direct simulations of compressible viscous flows. *J. Comput. Phys.* **101**, 104–129.

POPE, S. B. 2000 *Turbulent Flows*. Cambridge University Press.

RINGUETTE, M. J., WU, M. & MARTÍN, M. P. 2008 Coherent structures in direct numerical simulation of turbulent boundary layers at Mach 3. *J. Fluid Mech.* **594**, 59–69.

SCHLATTER, P. & ÖRLÜ, R. 2010*a* Assessment of direct numerical simulation data of turbulent boundary layers. *J. Fluid Mech.* **659**, 116–126.

SCHLATTER, P. & ÖRLÜ, R. 2010*b* Quantifying the interaction between large and small scales in wall-bounded turbulent flows: a note of caution. *Phys. Fluids* **22**, 051704.

SCHLATTER, P., ÖRLÜ, R., LI, Q., BRETHOUWER, G., FRANSSON, J. H. M., JOHANSSON, A. V., ALFREDSSON, P. H. & HENNINGSON, D. S. 2009 Turbulent boundary layers up to $Re_\theta = 2500$ studied through simulation and experiment. *Phys. Fluids* **21**, 051702.

SIMENS, M. P., JIMÉNEZ, J., HOYAS, S. & MIZUNO, Y. 2009 A high-resolution code for a turbulent boundary layers. *J. Comput. Phys.* **228**, 4218–4231.

SMITH, D. R. & SMITS, A. J. 1993 The simultaneous measurement of velocity and temperature fluctuations in the boundary layer of a supersonic flow. *Exp. Therm. Fluid Sci.* **7**, 221–229.

SMITH, M. W. & SMITS, A. J. 1995 Visualization of he structure of supersonic turbulent boundary layers. *Exp. Fluids* **18**, 288–302.

SMITS, A. J. & DUSSAUGE, J.-P. 2006 *Turbulent Shear Layers in Supersonic Flow*, 2nd edn. American Institute of Physics.

SMITS, A. J., MATHESON, N. & JOUBERT, P. N. 1983 Low-Reynolds-number turbulent boundary layers in zero and favourable pressure gradients. *J. Ship Res.* 147–157.

SMITS, A. J., SPINA, E. F., ALVING, A. E., SMITH, R. W. & FERNANDO, E. M. 1989 A comparison of the turbulence structure of subsonic and supersonic boundary layers. *Phys. Fluids* A **1**, 1865–1875.

SPINA, E. F., DONOVAN, J. F. & SMITS, A. J. 1991 On the structure of high-Reynolds-number supersonic turbulent boundary layers. *J. Fluid Mech.* **222**, 293–327.

SPINA, E. F. & SMITS, A. J. 1987 Organized structures in a compressible turbulent boundary layer. *J. Fluid Mech.* **182**, 85–109.

SPINA, E. F., SMITS, A. J. & ROBINSON, S. K. 1994 The physics of supersonic turbulent boundary layers. *Annu. Rev. Fluid Mech.* **26**, 287–319.

STOLZ, S. & ADAMS, N. A. 2003 Large-eddy simulation of high-Reynolds-number supersonic boundary layers using the approximate deconvolution model and a rescaling and recycling technique. *Phys. Fluids* **15** (8), 2398–2412.

SUPONITSKY, V., COHEN, J. & BAR-YOSEPH, P. Z. 2005 The generation of streaks and hairpin vortices from a localized vortex disturbance embedded in unbounded uniform shear flow. *J. Fluid Mech.* **535**, 65–100.

TOWNSEND, A. A. 1976 *The Structure of Turbulent Shear Flow*, 2nd edn. Cambridge University Press.

WARHAFT, Z. 2000 Passive scalars in turbulent flows. *Annu. Rev. Fluid Mech.* **32**, 203–240.

WU, X. & MOIN, P. 2009 Direct numerical simulation of turbulence in a nominally zero-pressure-gradient flat-plate boundary layer. *J. Fluid Mech.* **630**, 5–41.

XU, S. & MARTIN, M. P. 2004 Assessment of inflow boundary conditions for compressible turbulent boundary layers. *Phys. Fluids* **16** (7), 2623–2639.